Madelung Formalism Approach for Non-Local Nanoplamonics

by

Rúben Azinheira Alves

Thesis submitted for the degree of

Doctor of Philosophy

Metamaterials Research Group
School of Physics and Astronomy
University of Birmingham

2021

To my family

"Tell all the truth but tell it slant —
Success in Circuit lies
Too bright for our infirm Delight
The Truth's superb surprise
As Lightning to the Children eased
With explanation kind
The Truth must dazzle gradually
Or every man be blind —"

Emily Dickinson

Abstract

The main focus of this thesis is to provide an insight on modelling plasmonic systems. The recent advent of new fabrication techniques have pushed plasmonic systems further and further into the nanoscale. However, on one hand, the extreme confinement of plasmons can force them to exhibit some quantum properties that classical and macroscopic modelling of such systems simply fails to capture. On the other, plasmonic system are typically of the size that quantum models such as density functional theory, to give an example, are impractical due to the large number of interactions that need to be addressed. The more practical solutions is then the development of semi-classical models that keep the simplicity of the macroscale while addressing some of the quantum behaviour of plasmons.

In this thesis, I start by describing a classical, but valuable, tool to obtain the response of plasmonic systems analytically, called transformation optics. Then, I present a variation of the popular hydrodynamic Drude model, where I replace the fluid equations and their need for additional boundary conditions with a non-linear Schrödinger equation using the Madelung formalism. In order to prove that this new interpretation is valid, I push the non-local, non-linear Schrödinger equation into its linear and local limit and compare the results with full wave simulations and transformation optics. Then, I introduce a super-Gaussian potential into my equation in order to in-

troduce heuristically electron spill-out non-locality and compare the results with a popular non-local model readily available in the literature. With this comparison I am able to devise a fitting parameter and show that it is invariant on small changes of the geometry. With this proposed methodology, I was able to include the electron spill-out heuristically in a simple and modular method.

Contents

Chapter 1

Introduction

One of the most intringuing and active topics in photonics today is the use of localized surface plasmons in nanoscale structures. These structures can not only improve the sensing performance of photonic sensors [1–3], but also be adopted to improve other technologies exploiting light-matter interactions. Plasmonics has a wide range of applications for both theoretical work, for example the study of strong coupling [4, 5] and cavity optomechanics [6], among many others [7–10], and experimental and commercial applications such as photovoltaic technology [11] and nanoantennas [12–15]. However, modelling these mesoscopic structures has been an arduous path as the classical macroscopic theories often fail completely at these scales and their quantum description is impractical due to the size of the systems. Motivated by this modelling challenge, this thesis will reformulate the non-local hydrodynamic Drude model in terms of Madelung formalism that enables mesoscopic structures to be tractable while avoiding the need of defining additional boundary conditions seen in standard hydrodynamic Drude model approaches. In addition, we supplement this new approach with conformal transformation to have a solid theoretical framework.

The field of photonics is experiencing an exponential growth in the 21st century. Its objective is the study and manipulation of photons. In contrast, electronics and its advancements defined the 20th century. Plasmonics, as a field, is the junction of these two century defining technologies. It focuses on the interaction of electromagnetic fields and the free electrons in materials, such as metals and doped semiconductors. One of the most noteworthy advantages of photonic devices is that they can yield much faster data transmission rate, on the order of GHz, by exploiting light instead of radio-frequencies or microwaves [16]. Such high data rates are possible thanks to the optical fibre, which is undeniably the most accomplished photonic device along with the laser. Due to its characteristics, the optical fibre allows unprecedented data transmissions and telecommunications speed that is used worldwide. And so it became the backbone of the internet in recent times. For this reason, Sir Charles Kuen Kao was awarded the Nobel prize in 2009. However, the public demand for increasing performances requires the increase of the number of components in the same device. This can only be done by either continually increasing the sizes of our devices or by miniaturizing each component. Continually increasing the sizes of our devices is impractical at best. So, the only way forward is by miniaturizing each component. The continuous reduction of components' size in a photonic device is bounded by the fundamental barrier of the diffraction limit. Such fundamental limit states that light (in fact, any electromagnetic wave) cannot be confined to system whose dimensions are smaller than half its wavelength. For systems working at the 3rd telecom window, where the wavelength is at 1550 nm, the limit is 775 nm. This implies that the optical minimal limit is several times bigger than the tens of nm's sized devices produced from the state of the art electronic technology. With that in mind,

plasmonics emerges as a possible solution. Plasmonics relies on the coupling between free electrons and light. As a result, plasmonics is not bound by the diffraction limit mentioned and thus achieving sub-diffraction scales [17].

Plasmonics can be thought out as a hybrid between electronics and photonics as it retains the advantages of both of these fields. On one hand, plasmonics can yield fast data transference rates, much like photonics due to its light nature. On the other hand, it can be used on devices with sizes far below the diffraction limit just as semiconductor electronics. Even though plasmonics-based computer chips are still some years or even decades away, in the past few decades, plasmonics has evolved [18–25] tremendously with the development of technologies based on surface plasmon resonances that already have commercial applications. Namely, sensing is one of the most important application areas for plasmonics today [18, 26–28], with the pregnancy test as its greatest exponent [29].

1.1 Historical Background

The term "plasmon" accounts for a quasi-particle defined as a collective oscillation of the conduction electrons in a material, typically metals, excited by electromagnetic radiation. Plasmons are commonly treated as a macroscopic phenomena involving a high number of electrons occurring at high temperatures. However, recent studies have shown that such phenomena can exhibit quantum associated phenomena, such as photon-plasmons-photon entanglement [8–10, 30] and quantum tunnelling [31, 32].

In condensed matter, plasmons can be divided into two groups, namely volume (or bulk) plasmons and surface plasmon polaritons, or propagating surface plasmons [17]. Bulk plasmons result from the charge displacements in the interior of the material, while surface plasmons polaritons are charge

oscillations at the surface of the metal resonant with photons [33]. While bulk plasmons do not have many applications because their diminishing influence as devices are miniaturized, the study of surface plasmon polaritons is a very rich field, ranging from fundamental physics on the interaction of light and matter [34] to a myriad of applications that have emerged in the past decades that bridge physics with other sciences, namely biology [18, 20] and medicine [35]. So far, one of the great technological success of plasmonics is the improvement of optical sensors [36–38]. This is possible because plasmonic systems, yields a sub-wavelength field confinement and a field enhancement effects to the electromagnetic field that it interacts with. These plasmonic hot spots due to both effects can greatly increase the interactivity of the sensor with the sample. It is also worth mentioning particular achievements in other domains such as sub-wavelength focusing [39] and optical meta-materials (e.g. artificial materials whose electromagnetic properties are engineered not only by varying chemical composition, but also by the unit cell's shape, internal structure, position, orientation, etc.) [40] and even plasmons in graphene [41, 42]. Through these achievements, the field of plasmonics has been steadily increased both in size and relevance today. There are still many challenges to overcome when we attempt to downscale the material structures that support plasmons to the nanoscale, from the lack of a full quantum model to the proper and perfect way to build such small systems experimentally. This unstoppable miniaturization process will increase the sensitivity of optical sensors to unprecedented levels at the expense of fabrication complexity; and perhaps one day it will allow the replacement of electronics with a new generation of devices that are defined by their control of light instead of their control of electrons.

The basic treatment of light scattering was predominantly set by the

Mie's theory for the scattering and absorption of electromagnetic radiation by a dielectric sphere reported in 1908 [43]. This and the Drude model of free electrons proposed in 1900 [44], kicked-off plasmonics. To this day, these two theories still provide physical insight [45, 46] but they break down when trying to provide an accurate description for today's complex nanoparticles, as Mie's theory strictly applies only to circular and spherical nanoparticles and the Drude model does not account for quantum effects emerging at these scales.

The new type of complex plasmonic systems such as bowtie nanoantennas and nanoparticle-on-mirror nanocavities are able to produce strong light-matter interactions that can further increase the sensitivity and unlock other types of applications [47–50]. However there are many aspects of plasmons localised in nanometric and even picometric volumes that needed to be tackled, both from a theoretical and an experimental context. Initially, and for a long time, the classical description still satisfyingly described the majority of plasmonic systems. However, due to the unprecedented advancements of nano fabrication techniques and the advent of the nanoscaled systems, these classical models started to fall apart [51]. Due to the miniaturization, plasmonic systems started to show some quantum features which couldn't be explained by the classical models.

In order to solve this new problem, the field evolved into the development of semi-classical models [52]. These models try to address some quantum features of the plasmonic response while disregarding others. One should note that a full quantum description of a plasmonic system is yet to be developed as the size of the system renders the problem too convoluted for the computational resources available. With the development of semi-classical models, a clear division between local and non-local models was

made.

1.1.1 Local Models

Local models, also called classical models, assume that all the media in a plasmonic system can be described by an homogeneous media [53]. These media can be then characterized by only a frequency dependent dielectric function. The electromagnetic field is described using the Maxwell's equations, the metal is described with the Lorentz-Drude model and the environment is normally either air or vacuum for simplicity.

The main advantage of local models is their simplicity. For simple geometries (like planar, spherical and cylindrical interfaces between the metal and air), one needs only to impose explicitly the boundary conditions for the tangential electric field and the normal component of the displacement vector at the interface to have the full electrodynamic description of the system [13]. So the complications, and sophistication, of local models are brought from the geometry of the system [54].

There are numerous techniques to describe the plasmonic response of systems with a more complex geometry such as brute force numerical approach using methods like finite difference time domain, finite integration, method of moments, boundary element method, to name a few. However, I would like to highlight transformation optics. This technique applies mathematical transformations on the geometry of the system in order to simplify it. This simplification will then allow us to have an analytical solution [55, 56]. In a system where the third dimension can be collapsed (as it happens when it is infinite in that dimension), the transformations applied are conformal transformations (a two-dimensional transformation that is defined in the next chapter) wherein the in-plane materials properties are preserved

[53]. Because Maxwell's equations are conformal invariant, one can simplify the geometry of the system, solve it in this virtual world and the solution will also be the solution to the original geometry. This technique will be explained in depth in the next chapter as it forms the main lens through which a physical insight is provided on this thesis.

1.1.2 Non-Local Models

Contrary to local models, that take into account the electron-electron interactions with a damping mechanism, non-local models take these interactions into consideration directly. These interactions can be incorporated in a variety of semi-classical and quantum corrected models. The medium, mainly the metal, characterized by these models, although still homogeneous, is no longer only dependant on frequency but also dependant on every other electron of the system. One of the most noteworthy non-local model is the Hydrodynamic Drude model [52].

The Hydrodynamic Drude model (HDM) is a semi-classical model that describes the influence of the electromagnetic field on the electrons of the metal using the fluid equations. With these equations one can introduce a term called the Thomas-Fermi pressure that describes the electron-electron interactions of the system [57, 58]. This model will be described in detail along with a novel technique to solve it in chapter 3.

The novel methodology is the application of the Madelung formalism on the fluid equations used by the HDM. Initially, the Madelung formalism re-expressed the Schrödinger equation in terms of the fluid equations that describe the flow of probability of the wave function in quantum systems [59]. In this thesis, the objective is to provide an electrodynamic description of mesoscopic nanostructures by proceding in the oposite direction: the

fluid equations are re-written in one non-linear Schrödinger equation that is numerically tractable.

1.2 Structure of this Thesis

The remainder of the thesis is divided into four additional chapters:

Chapter 2 introduces and explains in detail transformation optics, which is used during this thesis with a twofold goal:

- to provide physical insight into the results and observations;
- as a local theory benchmark.

Chapter 3 presents the Hydrodynamic Drude model and how to associate it with the Madelung formalism.

Chapter 4 provides the results for the transformation optics technique, the Hydrodynamic Drude model and the Madelung formalism and a comparison between them in a local and non-local setting.

Chapter 5 provides some conclusions and possible future work.

Chapter 2

Transformation Optics

****

Parts of this Chapter are reproduced from **Rúben A. Alves**, Ariel Guerreiro, and Miguel Navarro-Cía, *Bridging the hydrodynamic Drude model and local transformation optics theory*, Phys. Rev. B 101, 235412, 2020 [60] and are noted appropriately in the text.

****

The propagation of light is not always done in a straight line. This can only happen in a vacuum. If one places a pen in a glass filled with water, it looks like the pen is bending. This happens due to the interface of water and air. Even in a seemingly homogeneous medium, like air, light might not propagate in a straight line due to effects like temperature. A mirage effect is an example of that; the hot sand induces a temperature gradient that in turn causes the refractive index of air to be inhomogeneous. In such a continuously varying medium, the ray path is a smooth curve that bends according to Fermat's principle. This shows that the refractive index of a material is directly related to the path that light takes. This is the

underlying principle of transformation optics.

Transformation optics apply coordinate transformations in order to, in a way, force light to take the path that one desires at the cost of engineering the material properties [61]. This, of course, can only be done mainly through the use of meta-materials, as their material properties can be tailored in order to achieve the results desired [62, 63].

Initially, transformation optics, and in particular conformal transformations, were applied in meta-materials in order to devise an invisibility cloak [64]. However, many of the devices designed using this approach demand complex and highly anisotropic meta-materials which makes the realisation of these materials challenging and, in many cases, practically impossible. Fortunately, there is a particular case of transformation optics where this challenge does not apply. In the particular case that one of the spatial dimensions can be collapsed, the transformations applied are conformal transformations. Because the Maxwell's equations are conformal invariant, when they are to be applied, then the in-plane material properties stay the same as the original as the tangential electric field ($E_{\perp}$) and the normal displacement field ($D_{/\!/}$) in the boundary of the materials are conserved. This facilitates the study of the structure's electromagnetic response.

2.1 Conformal Transformations

Conformal transformations have been widely used in both physics and engineering. This technique stems from the mathematics field of complex analysis and it enables finding the solution of many boundary problems by reshaping these boundaries. In engineering, conformal mapping has been used extensively in many disciplines. For instance, conformal transformations were used for airfoil theory and became a pratical tool for aerody-

namic design engineers [65]. Meanwhile, it underpinned the development of microwave planar technology [66, 67]. In physics, its use varies, from conformal field theory in quantum field theory to general relativity [68, 69]. Only in recent times, the electromagnetic community has resorted to this technique for metamaterials and plasmonics. In this document, we will focus more on their application on plasmonics.

A conformal transformation is a two-dimensional (2D) equivalent of the three-dimensional (3D) transformation optics in which orientation and angles are preserved locally. These transformations need to satisfy the Cauchy-Riemann conditions given by

$$\frac{\partial x}{\partial u} = \frac{\partial y}{\partial v} \tag{2.1}$$

and

$$\frac{\partial x}{\partial v} = -\frac{\partial y}{\partial u}, \tag{2.2}$$

where (x, y) are the coordinate system of the real world and (u, v) of the virtual one. So a conformal transformation should be a simple equation that transforms the set of coordinate system x, y in another coordinate system while also satisfying the Cauchy-Riemann conditions.

The main advantage of transformation optics (TO) is its simplicity. Assuming that the system under study has a possible transformation that both simplifies the geometry and satisfies Cauchy-Riemann conditions, that means that one is able to describe it analytically. One can also cascade transformation if the system in question has a slightly more complex geometry, as demonstrated later on this thesis. However, no matter how powerful this technique can be, it depends on the transformation applied. As we will

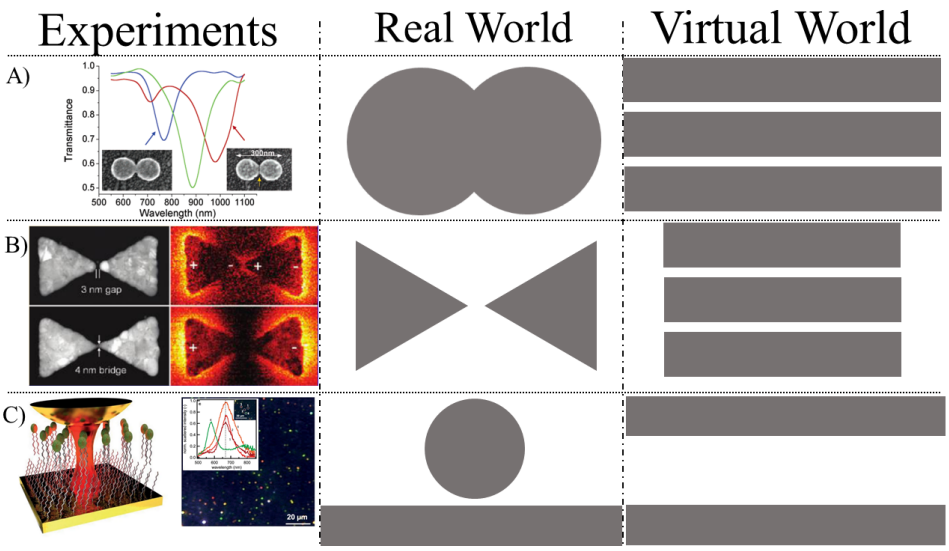

Figure 2.1 Illustrative examples of state-of-the-art fabricated nanoantennas (left), equivalent ideal physical model (center) and possible transformed space (right) for analytical analysis. A) Overlapping nanowires, image taken from [70]. B) Bowtie anoantennas, image taken from [71]. C) Particle on a mirror, image taken from [72].

see in the later chapters of this thesis, it might not be always worth applying the transformation. Generally, this happens if there is a geometry that cannot be transformed into a simpler one, or if there is a slight alteration of the geometry that invalidates the transformation. Luckily, plasmonics normally uses geometries where these transformations can be applied. In Fig. 2.1, three widely popular plasmonic system are presented: two overlapping nanowires (A) [60, 73], bowtie nanoantenna (B) [74–76] and nanoparticle on a mirror (C) [4, 23]. Not only transformation optics can be applied to these geometries but also slight variations as well [77]. Take for example, the two nanowires. If they are overlapping, then after two transformations (described later in this chapter), their geometry reverts back to the metal dielectric metal infinite periodic slab, depicted in Fig. 2.1A. However, if instead of being overlapping they would be separated, then, applying a dif-

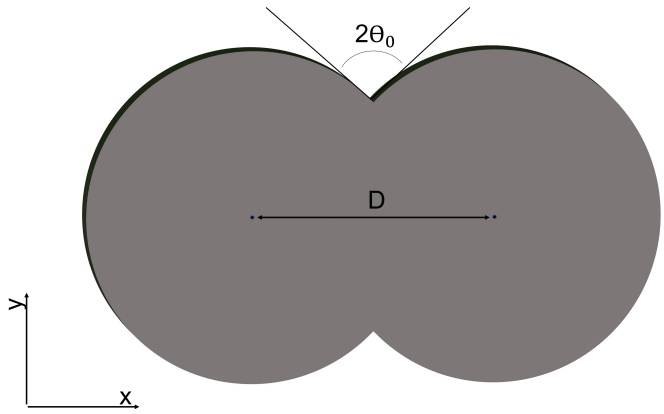

Figure 2.2 Schematic of the geometry suggested that can be treated in the quasi-static limit. The distance D is defined as the distance between the centres of each circle. The lines at the top represent the tangents of the vertex.

ferent transformation, its virtual world resembles that of the nanoparticle on a mirror with its two infinite metallic slabs [53, 56]. Another example would be the bowtie nanoantenna. In Fig. 2.1B, this geometry is represented with a gap between the two triangles. Because of this gap, the virtual world is composed of a metal-dielectric-metal periodic structure where the metal is finite on both ends. If instead the dimers of the bowtie touch at a single point, then the periodic structure would be semi-infinite instead [15].

2.2 Conformal Transformations for Plasmonics

In order to show an example of conformal transformations for plasmonics, let us assume the geometry of two overlapping nanowires; this system is one of the scenarios tackled with the Madelung formalism later in the thesis.

Fig. 2.2 represents overlapping nanowires proposed. The distance D is defined as the distance between the centres of the two wires and the illumination is done by a x-polarized plane wave. For it to be valid for the application of conformal transformations, it is assumed that the dimension

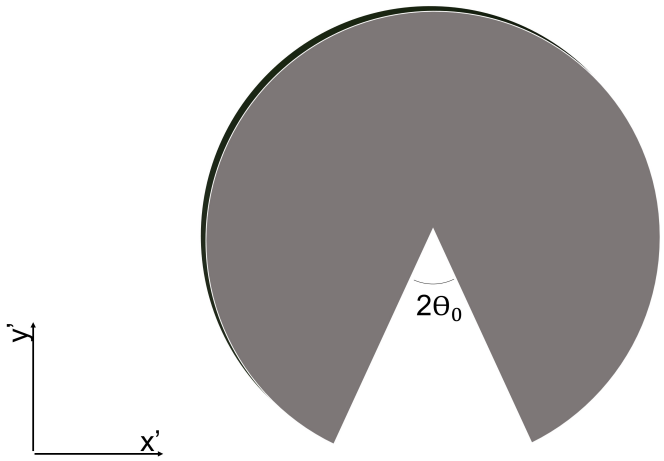

Figure 2.3 Schematic of the geometry suggested after the transformation from Eq. 2.3.

out of plane is infinite and homogeneous.

Defining $z = x + iy$,as the coordinates of the real world, then the overlapping nanowires can be morphed into a infinite periodic metal-insulator scenario by applying two transformations described in [60]. The first transformation is

$$z' = \frac{g^2}{z} - ir_0, \tag{2.3}$$

where r_0 defines the dipole position in the first virtual world (that is defined by the intensity of the electromagnetic field in real world), $z' = x' + iy'$ are the coordinates of the first virtual world, g is defined as $g^2 = 2r_0\sqrt{R^2 - \frac{D^2}{4}}$, where R and D are the radius and the distance between the centres of the nanowires, respectively.

It is easy to see that this transformation satisfies both Eq. 2.1 and Eq. 2.2. This allows us to change the geometry to the one presented in Fig. 2.3.

The final transformation that brings the original overlapping nanowires

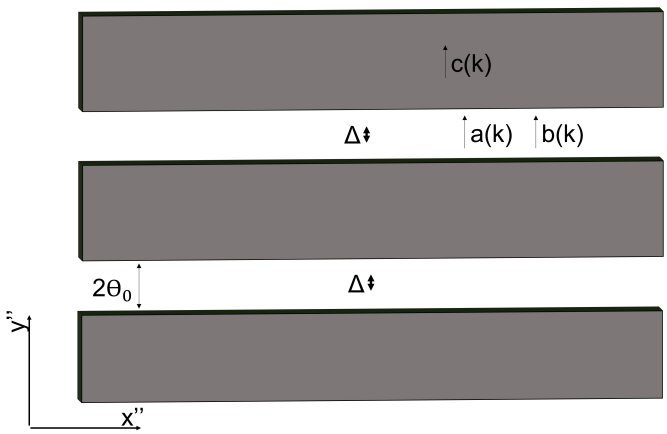

Figure 2.4 Schematic of the geometry suggested after the transformation from Eq. 2.4.

into a periodic metal-insulator scenario is

$$z'' = ln(\frac{z'}{r_0}), \tag{2.4}$$

where $z'' = x'' + iy''$ are the coordinates of the second virtual world, and complies with Eq. 2.1 and Eq. 2.2.

This second transformed space can be seen in Fig. 2.4. It is important to note that the shape represented is a periodic structure of metal-dielectric slabs. The uniform electric field, generated by the plane wave polarized along the dimer's axis, is transformed into series of dipoles. These dipoles are represented by the arrows Δ and their positions are characterized by the value of r_0; $2\theta_0$ is the angle at which the two circles cross sections join, see Fig. 2.2. Note that the orientation of the dipoles would be horizontal if the illuminating plane wave of the original space were polarized perpendicular to the dimer's axis.

The aim of this section is to compute the absorption cross section of the system. Due to the conformal transformation properties and the quasi-

static consideration, the power dissipation in the real and virtual worlds is the same. Thus, the absorption cross section of the real world is available by solving the simple electromagnetic problem found in the virtual world. To this end, the characteristic equation is first obtained by applying boundary conditions as described after this paragraph, which reproduces the derivation found in the Physical Review B paper [60]. The electric field generated by one of the dipoles is defined by the coefficient $a(k)$, where k is the wave number; the electric fields propagating on one of the slabs of air are defined by the coefficient $b(k)$ and the ones on one of the slabs of metal with $c(k)$, see Fig. 2.4.

The following is an edited version from the PhD candidate's peer reviewed paper [60].

From the tangential electric field boundary condition one has

$$a(k)e^{-k\theta_0} + b(k)(e^{-k\theta_0} - e^{k\theta_0}) = c(k)(e^{-k\theta_0} - e^{-k(2\pi-\theta_0)}) \tag{2.5}$$

and from the normal displacement field boundary condition one has

$$a(k)e^{-k\theta_0} + b(k)(e^{-k\theta_0} + e^{k\theta_0}) = \varepsilon c(k)(e^{-k\theta_0} + e^{-k(2\pi-\theta_0)}). \tag{2.6}$$

In order to have the same angle on the right hand side of the system one has to multiply both Eqs. 2.5 and 2.6 by $e^{-k\pi}e^{k\pi}$

$$a(k)e^{-k\theta_0} + b(k)(e^{-k\theta_0} - e^{k\theta_0}) = c(k)e^{-k\pi}(e^{k(\pi-\theta_0)} - e^{-k(\pi-\theta_0)}) \tag{2.7}$$

$$a(k)e^{-k\theta_0} + b(k)(e^{-k\theta_0} + e^{k\theta_0}) = \varepsilon c(k)e^{-k\pi}(e^{k(\pi-\theta_0)} + e^{-k(\pi-\theta_0)}). \tag{2.8}$$

By dividing Eq. 2.7 with Eq. 2.8 yields

$$\varepsilon\frac{a(k)e^{-k\theta_0}+b(k)(e^{-k\theta_0}-e^{k\theta_0})}{a(k)e^{-k\theta_0}+b(k)(e^{-k\theta_0}+e^{k\theta_0})}=\tanh\left(k(\pi-\theta_0)\right). \tag{2.9}$$

Organizing this last equation and isolating $b(k)$ one has

$$b(k)=\frac{a(k)e^{-k\theta_0}}{2}\frac{\varepsilon-\tanh\left(k(\pi-\theta_0)\right)}{\cosh\left(k\theta_0\right)[\varepsilon\tanh\left(k\theta_0\right)+\tanh\left(k(\pi-\theta_0)\right)]}. \tag{2.10}$$

With the definition of $b(k)$ one can replace it in Eq. 2.7 to define

$$c(k)=\frac{a(k)}{2}\frac{e^{k\pi}e^{-k\theta_0}}{\cosh\left(k(\pi-\theta_0)\right)}\left(\varepsilon\frac{\tanh\left(k\theta_0\right)+1}{\varepsilon\tanh\left(k\theta_0\right)+\tanh\left(k(\pi-\theta_0)\right)}\right). \tag{2.11}$$

Which simplified leads to

$$c(k)=\frac{a(k)}{2}\frac{\varepsilon e^{k\pi}}{\cosh\left(k\theta_0\right)\cosh\left(k(\pi-\theta_0)\right)}\frac{1}{\varepsilon\tanh(k\theta_0)+\tanh\left(k(\pi-\theta_0)\right)}. \tag{2.12}$$

The dispersion relation can then be found when $b(k)$ and $c(k)$ diverge which means that

$$\varepsilon\tanh\left(k\theta_0\right)=-\tanh\left(k(\pi-\theta_0)\right). \tag{2.13}$$

The dispersion relation dictates the relationship between ω and k. With this relationship defined, one can now deduce the electric field

$$\vec{E}(z=iy_n)=-i\frac{\Delta}{2\varepsilon\theta_0}\Gamma k, \tag{2.14}$$

where y_n is the position of the nth dipole, Δ is the dipole [60]. Γ is defined

by

$$\Gamma = \frac{\varepsilon \cosh^{-1}(k\theta_0) e^{-k\theta_0}[1 + \tanh(k\theta_0)]}{\varepsilon - \varepsilon_c + \varepsilon(\varepsilon\varepsilon_c - 1)\tanh^2(k\theta_0)} \tag{2.15}$$

where $\varepsilon_c = \frac{\theta_0 - \pi}{\theta_0}$ [60].

With this one can derive the absorption cross section in the quasi-static approximation by first defining the dissipated power

$$P_a = -\frac{\omega}{2}\Im\{\Delta^* e_x \cdot \vec{E}(z'' = iy_n'')\} \tag{2.16}$$

and then defining the absorption cross section as

$$\sigma_a = \frac{P_a}{P_i n} = 2\pi^2 k_0 \frac{\Sigma^2}{\theta_0}\Re(k\Gamma), \tag{2.17}$$

where $\Sigma = D\sin(\theta_0)$ [60].

As stated previously, Eq. 2.17 is the absorption cross section of the geometry defined in Fig. 2.4, which, because Maxwell's equations are conformal invariant, implies that it is also the absorption cross section of the geometry defined in Fig. 2.2. This is the power of transformation optics, where by solving a much more simplified geometry analytically, one can have the solution of a complex geometry. In Chapter 4, I will show the result and compare with a full wave simulation.

Chapter 3

Hydrodynamic Drude Model and the Madelung Formalism

****

Section 3.3 of this Chapter is an edited version from **Rúben A. Alves**, Ariel Guerreiro, and Miguel Navarro-Cía, *Bridging the hydrodynamic Drude model and local transformation optics theory*, Phys. Rev. B 101, 235412, 2020 [60].

****

3.1 Drude Model

The simplest way to describe a gas is to assume that each particle of the gas is an identical solid sphere that moves in a straight line until it collides with another. Aside from the collisions, no other forces act on the particles and the time taken by each collision is negligible. In 1900, Drude used a variation of this model to describe the free electrons on a metal. In the

simplest gasses, there is only one kind of particle. In the metal, however, there needs to be two types of charges, the free electrons and the nucleons [44]. Drude then postulated that the electrons in the valence band in a metal (can also be referred as free electrons) became detached and are able to move freely, while the much heavier and immobile metallic ions remain intact to form the structure of the metal.

The Drude model treats the dense free electron gas in metals with the kinetic theory of gasses by slightly modifying it to account for the electron-electron and the electron-ion interactions. In order to do this, one needs to make some assumptions [44]. First, these interactions are neglected during collisions. Thus in the absence of an external field, each electron moves uniformly in a straight line. The collisions, themselves, have to be characterized as an instantaneous event that alter the velocity of the electrons. These collisions have a probability per unit of time of $\frac{1}{\tau}$. τ is known as the relaxation time and follows the assumption that any given electron in a metal will, on average, travel for τs between each collision. This relaxation time is most commonly characterized as a damping mechanism defined as $\gamma = 1/\tau$ that will account for the electron-ion interactions. Lastly, these collisions are assumed to be elastic collisions in order to maintain local thermodynamic equilibrium. Fig. 3.1 shows the trajectory of a conduction electron in a metal according to these assumptions.

With these assumptions in place, one can use the equations of motion to characterize the movement of the electrons in a metal under a displacing charge carrier force described by the electric field E.

$$m_e \frac{d^2 r}{dt^2} = -eE - m_e \gamma \frac{dr}{dt}, \tag{3.1}$$

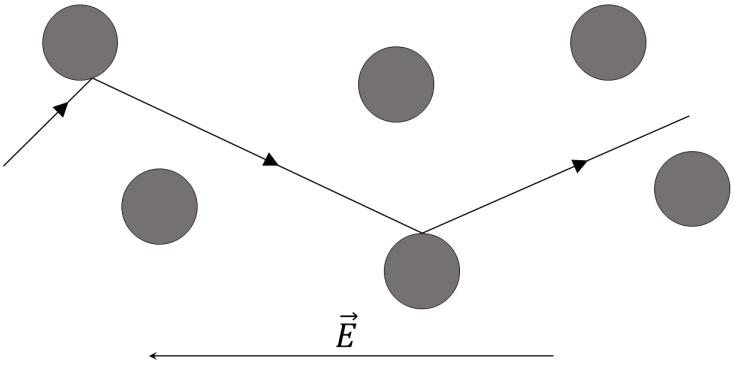

Figure 3.1 Schematic of the trajectory of a conduction electron under the influence of an electric field according to the Drude model

where m_e is the effective mass of the free electrons, e is the electron charge and γ is the damping constant. Assuming that $r(t) = \mathbb{R}\{r(\omega)e^{-i\omega t}\}$ and $E(t) = \mathbb{R}\{E(\omega)e^{-i\omega t}\}$ leads to

$$(-m_e\omega^2 - im_e\omega\gamma)r(\omega) = eE(\omega), \tag{3.2}$$

Assuming that the polarization is given by the formation of n dipoles per unit volume, then the polarization takes the form of

$$P = ner(\omega) \tag{3.3}$$

that connects to the electric field following

$$\epsilon_0\chi^{(1)}(\omega)E(\omega) = P. \tag{3.4}$$

Then from Eqs. 3.1, 3.3 and 3.4 one gets

$$\chi^{(1)} = -\frac{ne^2}{\epsilon_0 m_e\omega(\omega + i\gamma)} \tag{3.5}$$

From Eq. 3.5 one can extract the dielectric function

$$\varepsilon(\omega) = 1 + \chi^{(1)}(\omega) = 1 - \frac{\omega_p^2}{\omega(\omega + i\gamma)}, \tag{3.6}$$

with $\omega_p = \sqrt{\frac{e^2 n}{m_e \epsilon_0}}$.

With Eq. 3.6, the Drude model can be used to describe a metallic region on the Maxwell's equations defining the classical model for plasmonics [78]. Even to this day, a variation of this model, the Lorentz-Drude model, is still the preferred model used to describe a plasmonic system. However, at the nanometric scale, the quantum behaviour of the electrons, such as tunnelling and entanglement to name a few, starts to emerge. In order to address this a new model had to be introduced. This new model is called the hydrodynamic Drude model, that will be discussed in the next section.

3.2 Hydrodynamic Drude Model

The last decade has shown an unprecedented growth of the field of plasmonics due to the advancements of nanofabrication techniques and imaging [57, 79–82]. However, with these advances, a problem kicks off; the classical description for plasmonics can, when applied at the nanometre scale, become insufficient to describe these systems [50, 83]. Similarly, quantum electrodynamics are still prohibitive for such mesoscopic systems due to the amount of interactions that such a model needs to account for, as a full quantum model would need to describe each electron in the system as well as their interactions, leading to a complex many-body problem [84]. In order to solve this problem, a new model, the Hydrodynamic Drude model (HDM), was introduced. The HDM is a semi-classical model that uses the fluid equation to describe the electrons in a metal under the influence of

electromagnetic fields [85, 86]. While the Drude model assumes that the electrons are a point charge that move uniformly while colliding with the immovable ions, the HDM assumes that the electrons behave like a fluid [52]. With this one can now describe some quantum phenomena while still holding some of the simplicity of the classical models [86].

The main advantages of the HDM are that it takes into account atomic and subatomic interactions, in particular electron-electron repulsion by considering the Pauli exclusion principle and the fact that it also has the ability to be a non-local model [87–89]. This model has been used to modulate the response of plasmonic nanostructures and has shown a good agreement with the experimental data [86].

3.2.1 The Continuity and the Euler Equations

In order to apply the HDM to a plasmonic system, one needs to pay attention to two particularly important equations. First the continuity equation

$$-\partial_t n = \nabla \cdot (n\vec{u}) \tag{3.7}$$

where n is the electron density and $\vec{u}$ is electron velocity. The current density can also be introduced as $\vec{j_n} = n\vec{u}$. Eq. 3.7 dictates the conservation of the number of particles and charge in the system.

The other important equation is the Euler equation. If one states the the total force acting on a volume is equal to the surface integral of this volume over the pressure, then

$$-\oint\!\!\!\!\!\!\diagup_S p\, dS = -\int_V \nabla p\, dV \tag{3.8}$$

where p is the pressure of the liquid, S is the surface of the volume V and

S is theis normal unit vector. The force per volume takes the form

$$m_e n \frac{d\vec{u}}{dt} = -\nabla p, \tag{3.9}$$

where m_e is the electron mass. The total derivative in Eq. 3.9 can be written as

$$\frac{d\vec{u}}{dt} = \frac{\partial \vec{u}}{\partial t} + \frac{dx}{dt}\frac{\partial \vec{u}}{\partial x} + \frac{dy}{dt}\frac{\partial \vec{u}}{\partial y} + \frac{dz}{dt}\frac{\partial \vec{u}}{\partial z} = \frac{\partial \vec{u}}{\partial t} + (\vec{u}\cdot\nabla)\vec{u}. \tag{3.10}$$

From Eq. 3.9 one can add an electromagnetic driving force, and a lossy term defined by $\Gamma = \gamma n \vec{u}$ and the changes presented in Eq. 3.10 to transform Eq. 3.9 into

$$n\partial_t \vec{u} + n(\vec{u}\cdot\nabla)\vec{u} = -\frac{ne}{m_e}(\vec{E} + \vec{u}\times\vec{B}) - \frac{\nabla P}{m_e} - \gamma n\vec{u}, \tag{3.11}$$

where $\partial_i = \frac{\partial}{\partial i}$, e is the electron charge, $\vec{E}$ and $\vec{B}$ are the electric and magnetic fields of the electromagnetic radiation, and γ is a phenomenological parameter that represents the damping due to electron-ion collisions. With Eq. 3.11, one has defined the two equations necessary to implement the HDM. In the next subsection, I will go in more detail on the pressure term presented in the equation in the next subsection.

3.2.2 Thomas-Fermi Pressure

As stated previously, the HDM is a semi-classical model that describes the metallic regions of a plasmonic system as charge fluid. This fluid has also a characteristic pressure. This is called the Thomas-Fermi pressure and accounts for the electron-electron interactions and the Pauli exclusion principle, [90, 91]. In an uniform electron gas, where there are N electrons in

a given volume V, with a density of $n = \frac{N}{V}$, at temperature $T = 0$, the electrons will occupy all states up to the Fermi level. This means that the occupied volume of phase space is given by this sphere

$$V_p = \frac{4}{3}\pi p_f^3 V, \tag{3.12}$$

where p_f is the Fermi momentum. Under the Pauli exclusion principle, two electrons can occupy a volume of h^3, where h is the Planck's constant. This means

$$n = \frac{N}{V} = \frac{2}{h^3}\frac{4}{3}\pi p_f^3, \tag{3.13}$$

which implies that

$$p_f = \hbar k_f = \hbar\Big(3\pi^2 \frac{N}{V}\Big)^{\frac{1}{3}}. \tag{3.14}$$

The total kinetic energy K for N electrons with momenta $\vec{p_i}$ is given by

$$K = \sum_{i=1}^{N} \frac{p_i^2}{2m_e}. \tag{3.15}$$

In the sphere in the momentum space, the sum is transformed into the integral $\sum_k \rightarrow \frac{V}{(2\pi)^3}\int 4\pi k^2 dk$. So Eq. 3.15 for the two electrons (with different spins) takes the form

$$K = \sum_{|K|\leq k_f} \frac{p^2}{2m_e} = 8\pi \frac{V}{(2\pi)^3}\frac{\hbar^2}{2m_e}\int_0^{k_f} k^4 dk = \frac{3}{10}\frac{\hbar^2}{m_e}(3\pi^2)^{\frac{2}{3}}\frac{N^{\frac{5}{3}}}{V^{\frac{2}{3}}}. \tag{3.16}$$

In order to obtain the Thomas-Fermi pressure one need to just differen-

tiate with respect to volume to get

$$P = (3\pi^2)^{2/3}\frac{\hbar^2}{5m_e}n^{5/3}. \tag{3.17}$$

3.3 Madelung Formalism

Note that the following is an edited version from [60].

Originally, Madelung established this formalism to transform the Schrödinger equation into the fluid equations. In this way, these fluid equations would describe the flow of probability of the wave function in quantum systems [59]. In this thesis, however, I proceed in the opposite direction. Using the established link between these equations, one can rewrite the fluid equations as a non-linear Schrödinger equation that we can solve numerically [60, 92]. Unlike the standard HDM approaches found in the literature [86], the approach described in this thesis does not rely on the definition of additional boundary conditions to describe the system, which are to this day a contested subject. Following this approach, one defines the geometry with the linear terms of the potential in the Schrödinger equation.

Having a Schrödinger equation to describe the system, instead of a system for the fluid equations, allows for the use of methods that are more commonly found in the field of quantum mechanics and quantum optics. The use of these methods will allow us to navigate the problem. Additionally, this will formalize the analogy between plasmonic systems and meta-atoms even further; previously, the analogy was only due to the collective behaviour of the electrons in the metal that could be discretized into modes much like the electron bounds in the atom. Now, however, one can use even the same equations and methods to describe these two different phenomena (i.e. an electron trapped in a potential well and the collective oscillations of

conduction electrons in a metal nanoparticles).

As previously stated the Madelung formalism was initially established in order to understand the Schrödinger equation better by transforming it into the fluid equations. So, starting from the Schrödinger equation

$$i\hbar\alpha\partial_t\psi = \left[-\frac{\hbar^2\beta}{2m_e}\nabla^2 + V\right]\psi, \tag{3.18}$$

where α and β are normalising constants in order to transform Eq. 3.18 into Eqs. 3.7 and 3.11, it is also necessary to assume that the solution to this Schrödinger equation takes the form of $\psi = n^{1/2}e^{i\mathcal{S}}$. With this assumption,

$$\partial_t\psi = \frac{1}{2}\frac{\dot{n}}{n^{1/2}}e^{i\mathcal{S}} + i\dot{\mathcal{S}}n^{1/2}e^{i\mathcal{S}} \tag{3.19}$$

and

$$\nabla^2\psi = (\partial_x^2 + \partial_y^2)\psi, \tag{3.20}$$

where

$$\partial_r\psi = \frac{1}{2}\frac{\partial_r n}{n^{1/2}}e^{i\mathcal{S}} + i\partial_r\mathcal{S}n^{1/2}e^{i\mathcal{S}} = n^{1/2}e^{i\mathcal{S}}\left(i\partial_r\mathcal{S} + \frac{\partial_r n}{2n}\right), \tag{3.21}$$

with $r = x, y$. Hence,

$$\partial_r^2\psi = \left[\frac{1}{2}\frac{\partial_r^2 n}{n} - \frac{1}{2}\left(\frac{\partial_r n}{n}\right)^2 + i\partial_r^2\mathcal{S}\right]n^{1/2}e^{i\mathcal{S}} + \left(\frac{1}{2}\frac{\partial_r n}{n} + i\partial_r\mathcal{S}\right)^2 n^{1/2}e^{i\mathcal{S}}. \tag{3.22}$$

With this Eq. 3.20 takes the form

$$\nabla^2\psi = \left[\frac{1}{2}\frac{\nabla^2 n}{n} - \frac{1}{4}\left(\frac{\nabla n}{n}\right)^2 - (\nabla\mathcal{S})^2 + i\nabla^2\mathcal{S} + i\frac{\nabla n\nabla\mathcal{S}}{n}\right] n^{1/2}e^{i\mathcal{S}}. \quad (3.23)$$

Replacing this back into Eq. 3.18 and separating the real part and the imaginary part one has

$$-\hbar\alpha\dot{\mathcal{S}} = -\frac{\hbar^2\beta}{2m_e}\left[\frac{1}{2}\frac{\nabla^2 n}{n} - \frac{1}{4}\left(\frac{\nabla n}{n}\right)^2 - (\nabla\mathcal{S})^2\right] + V \quad (3.24)$$

for the real part, and

$$\frac{\hbar\alpha}{2}\dot{n} = \left[-\frac{\hbar^2\beta}{2m_e}\left(\nabla^2\mathcal{S} + \frac{\nabla n\nabla\mathcal{S}}{n}\right)\right] n \quad (3.25)$$

for the imaginary part.

Assuming that $\nabla\mathcal{S} = u$ (which has a small repercussion in the context of electromagnetism that will be outlined in more detail in the next page), Eq. 3.25 transforms into

$$\dot{n} = -\frac{\beta}{\alpha}\frac{\hbar}{m_e}\nabla\cdot(nu). \quad (3.26)$$

Comparing Eq. 3.7 with Eq. 3.26 yields that

$$\frac{\beta}{\alpha}\frac{\hbar}{m_e} = 1. \quad (3.27)$$

From Eq. 3.25, one has

$$-\dot{\mathcal{S}} = -\frac{\beta}{\alpha}\frac{\hbar}{2m_e}\left[\frac{1}{2}\frac{\nabla^2 n}{n} - \frac{1}{4}\left(\frac{\nabla n}{n}\right)^2 - (\nabla\mathcal{S})^2\right] + \frac{1}{\alpha\hbar}V \quad (3.28)$$

defining $V = V' - \beta V_B$, where

$$V_B = -\frac{\hbar^2}{4m_e}\left[\frac{\nabla^2 n}{n} - \frac{1}{2}\left(\frac{\nabla n}{n}\right)^2\right] = -\frac{\hbar^2}{4m_e}\frac{\nabla^2\sqrt{n}}{\sqrt{n}} \tag{3.29}$$

is the Bohm potential. With this in mind, and considering again that $\nabla\mathcal{S} = u$, Eq. 3.26 simplifies to

$$-\dot{u} = \frac{\beta}{\alpha}\frac{\hbar}{2m_e}\nabla(u\cdot u) + \frac{1}{\alpha\hbar}\nabla V'. \tag{3.30}$$

Rearranging Eq. 3.30, one has

$$n\vec{u} + n(\vec{u}\cdot\nabla)\vec{u} = -\frac{m_e}{\beta\hbar^2}n\nabla V'. \tag{3.31}$$

Comparing this equation to the original fluid equation, yields

$$\nabla V' = \frac{\beta\hbar^2 e}{m_e^2}\vec{E} + \frac{\beta\hbar^2}{m_e^2}\frac{1}{n}\nabla P + \gamma\frac{\beta\hbar^2}{m_e}\vec{u} + \frac{\beta\hbar^2}{m_e^2}\nabla\mathcal{U}, \tag{3.32}$$

where $\vec{E}$ is the electric field, P is the Thomas-Fermi pressure, γ loss coefficient and $\mathcal{U}$ the confining potential that defines the geometry of the system without the need to have additional boundary conditions. Earlier, it was assumed that $\nabla\mathcal{S} = u$. This means that the magnetic interaction (that is governed by $\vec{u}\times\vec{B}$) is neglected. This is common in plasmonics since the magnetic part of an electromagnetic wave is substantially smaller than its electric counterpart.

Assuming a perfect metal with no losses, the potential takes the form of

$$V = \frac{\beta\hbar^2 e}{m_e^2}\vec{r}\cdot\vec{E} + \frac{\beta\hbar^2}{m_e^2}\frac{(3\pi^2)^{2/3}\hbar^2}{2m_e}n^{2/3} + \frac{\beta\hbar^2}{m_e^2}\mathcal{U} + \beta\frac{\hbar^2}{4m_e}\frac{\nabla^2\sqrt{n}}{\sqrt{n}}. \tag{3.33}$$

The definition $\psi = n^{1/2}e^{i\mathcal{S}}$ implies that $n = N_0|\psi|^2$, which means that the full potential on the Schrödinger equation takes the form

$$V = \frac{\beta\hbar^2 e}{m^2}\vec{r}\cdot\vec{E} + \frac{\beta\hbar^2 e}{m_e^2}\mathcal{U}[eV] + \frac{\beta\hbar^2}{m_e^2}\frac{(3\pi^2)^{2/3}\hbar^2 n_0^{2/3}}{2m_e}|\psi|^{4/3} + \beta\frac{\hbar^2}{4m_e}\frac{\nabla^2\sqrt{|\psi|^2}}{\sqrt{|\psi|^2}}. \tag{3.34}$$

Eq. 3.34 shows the full potential needed to completely describe a plasmonic system using the HDM with a Schrödinger equation. The first two terms are linear: the first one describes the interaction of the electric field with our system (in order to do this transformation, one had to assume that the magnetic field is negligible), while the second one determines the geometry used. The other two terms in Eq. 3.34 are non-linear. The first of these comes from the Thomas-Fermi pressure while the last one is the Bohm potential, a virtual potential introduced in the Schrödinger equation so that it can be transformed into the fluid equations. From now on, these potentials will be divided into three groups. H_0 will be given by

$$H_0 = -\frac{\hbar^2\beta}{2m_e}\nabla^2 + \frac{\beta\hbar^2 e}{m_e^2}\mathcal{U}[eV] \tag{3.35}$$

so that

$$H_0\,|i\rangle = \lambda\,|i\rangle\,, \tag{3.36}$$

where $|i\rangle$ forms a base of solutions to the Schrödinger equations as if there was no electromagnetic field to interact. The interaction term of the electromagnetic field is going to be housed in the interaction Hamiltonian as

$$H_I = \frac{\beta\hbar^2 e}{m_e^2}\vec{r}\cdot\vec{E}. \tag{3.37}$$

The non-linear terms can then be inside their own Hamiltonian

$$H_{NL} = \frac{\beta\hbar^2}{m_e^2}\frac{(3\pi^2)^{2/3}\hbar^2 N^{2/3}}{2m_e}|\psi|^{4/3} + \beta\frac{\hbar^2}{4m_e}\frac{\nabla^2\sqrt{|\psi|^2}}{\sqrt{|\psi|^2}}. \tag{3.38}$$

One should note that in order to implement this model for this thesis, I have neglected this non-linear Hamiltonian by linearising Eq. 3.34. This is a common procedure in the HDM. However, instead of linearising the implementation of the additional boundary conditions, my approach linearises the potential, which in the end accomplishes the same result.

After having the fluid equations used in the HDM re-written into a Schrödinger equation; and having the Hamiltonian of that Schrödinger equation well defined, one only needs to have a quantum mechanical/ quantum optics mechanism comparable to the macroscopic absorption cross section to be able to compare the model presented here to the ones found in the literature. Initially, due to the demonstrated analogy between plasmonic systems and an electron trapped in a potential well, this thesis uses used the Rabi oscillations.

Rabi Oscillations

The Rabi oscillations describe the interaction of a two level atom with an electromagnetic field. Assuming that the field is tuned to the transition between two plasmon modes, the wave function can be written as

$$\psi = C_a\varphi_a + C_b\varphi_b. \tag{3.39}$$

It is then possible to write Eq. 3.18 as [60]

$$\partial_t \begin{bmatrix} C_a \\ C_b \end{bmatrix} = -i \begin{bmatrix} \Omega_{AA}(t) & \Omega_{AB}(t) \\ \Omega_{BA}(t) & \Omega_{BB}(t) \end{bmatrix} \begin{bmatrix} C_a \\ C_b \end{bmatrix}. \tag{3.40}$$

This result is formally analouge to the Bloch equations derived in quantum optics. This strengthens the analogy made so far, as the solutions to Eq. 3.40 can be found following the approach developed in the context of quantum optics. The absorption coefficient (which would be the quantum mechanical analogous property to the absorption cross section) can be calculated by recasting Eq. 3.40 in the interaction picture, obtaining [93, 94]

$$\partial_t \begin{bmatrix} C_a \\ C_b \end{bmatrix} = -i \begin{bmatrix} 0 & \Omega(t) \\ \Omega^*(t) & 0 \end{bmatrix} \begin{bmatrix} C_a \\ C_b \end{bmatrix}, \tag{3.41}$$

with $\Omega(t) \equiv \Omega_{A,B}$.

Applying the rotating wave approximation, $\Omega(t)$ is

$$\Omega(t) \approx \frac{\Omega_0}{2} e^{i(\omega-\omega_0)t} = \frac{\Omega_0}{2} e^{i\Delta t}, \tag{3.42}$$

where $\Delta = (\omega - \omega_0)$ is the detuning between the field frequency ω_0 and the natural frequency of the transition of the energy levels.

This means that

$$|C_b(t)|^2 = \frac{\Omega_0^2}{\Omega'^2} \sin^2\left(\frac{\Omega' t}{2}\right), \tag{3.43}$$

where $\Omega' = \sqrt{\Omega_0^2 + \Delta^2}$ and $\Omega_0 = \langle A| H_I |B\rangle$ where A and B are the two energy levels. Eq. 3.43 represents the probability of an electromagnetic wave, with frequency ω, to excite the system from the state $|A\rangle$ to the state

$|B\rangle$ by absorbing a photon. This probability oscillates over time. However, its average value, $\frac{\Omega_0^2}{2\Omega'^2}$, would correspond to the probability of a photon being absorbed thus making a close parallel to the absorption cross section, which is a macroscopic property of the system.

One should note that this method is just a first order approximation as there is no clear approach to map the absorption cross section, a macroscopic property of a system, to its microscopic relationships. There is, however, a method that can be implemented that can improve this approximation. This is the Fermi's golden rule that is going to be discussed in the next section.

Fermi's Golden rule

In the Fermi's golden rule, perturbation theory is used to calculate the probability of a transition from one eigenstate to a continuum of eigenstates of a quantum system per unit time. If the strength of the perturbation is independent of time, then this transition rate is time invariant as well. The transition rate is proportional to the strength of the coupling between the initial and final states of the system and the density of states. This rule can also be applied if the final state is discrete, and not part of a continuum, if one accounts for decoherence processes such as relaxation or collision of the atoms. In this case, instead of a density of states, the system is governed by the reciprocal of the decoherence bandwidth.

Assuming that the solution to the time dependent Schrödinger equation takes the form $|\psi(t)\rangle = \sum_n a_n(t) e^{-iE_n t/\hbar} |n\rangle$ then

$$H |\psi(t)\rangle = i\hbar \partial_t |\psi(t)\rangle \tag{3.44}$$

can be written as the following

$$\Big(H_0 + H_I - i\hbar\partial_t\Big) \sum_n a_n(t) \left|n\right\rangle e^{-iE_n t/\hbar} = 0 \tag{3.45}$$

By expanding and applying the time derivative to Eq. 3.45 and finally by applying a $|k\rangle$ then Eq. 3.45 transforms into

$$i\hbar \frac{da_k(t)}{dt} = \left\langle k\right| H_I \left|n\right\rangle e^{i(E_k - E_n)t/\hbar}. \tag{3.46}$$

This implies that

$$a_k(t) = -\frac{2\pi}{\hbar} \int_0^t \left\langle k\right| H_I \left|n\right\rangle e^{i\omega_k t/\hbar} dt. \tag{3.47}$$

This means that for a system with two discrete energy states, the Fermi's golden rule can be written as

$$\sigma_a = \frac{2\pi}{\hbar^2} \left\langle f\right| H_I \left|i\right\rangle g(w), \tag{3.48}$$

where $|i\rangle$ and $|f\rangle$ are solutions to the Schrödinger equation with only H_0. The function $g(w)$ represents the density of states at the energy E_f and it will be assumed to be 1 in this thesis. This means that one should consider that the power transferred from the light to the plasmonic system is constant.

3.3.1 Local and Non-Local Potentials

To end this chapter, there is one more detail that I would like to discuss. Depending on the way that one defines the potential $\mathcal{U}[eV]$ in Eq. 3.34 one can impose the local limit to the model described above or impose non-localities in the system (e.g. electron spill-out). This thesis illustrates the

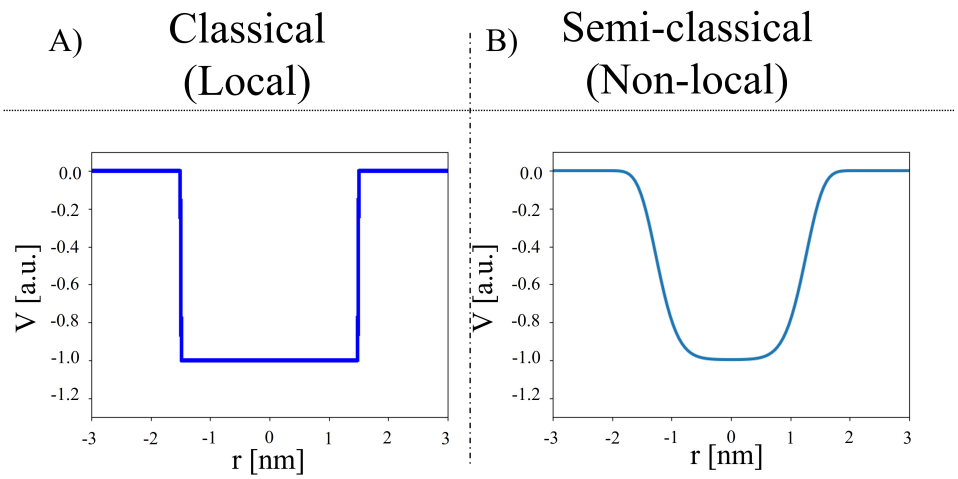

Figure 3.2 Representations of the two cases of potentials studied. A) the classical limit of the model, where the potential well is defined with a sharp boundary. B) non-local approach where the potential well is defined with super-Gaussians.

analytical model laid down with two types of potentials.

For the first type, the potential $\mathcal{U}$ is a rigid well. The walls of this well go from 0 *a.u.* to 1 *a.u.* in one computational cell, represented in Fig. 3.2A. This pushes the model to the local-response approximation since such well yields a constant equilibrium electron density in the absence of field excitation inside the metal and a Dirac delta function centred at the metal surface for the incident field induced charge density. The original HDM uses additional boundary conditions in order to define the geometry and the system's non-locality. With the Madelung formalism, I can postulate that the walls of the well are described using a super-Gaussian. If instead of a rigid wall, one defines the boundary of the system with super-Gaussians (see Fig. 3.2B), the equilibrium electron density exponentially decaying across the metal surface is modelled. Hence, the electron spill-out would inherently be captured heuristically [89, 95, 96]. It is worth pointing out that such super-Gaussian boundary will be able to account for the inducing charges smearing outside

the metal-air interface, but will exclude those induced charges inside the metal as the equilibrium electron density does not oscillate inside the metal, close to the metal-air interface. This latter feature would be retained if the Schrödinger-Madelung equation were not linearised and is left as future work.

Fig. 3.3 presents a flowchart of the python script used to solve both of the potentials presented here. It also provides a high level detail of the various tests that the script carries out to output converged physically-meaningful results. In the next chapter while presenting the results, the two type of potentials will be discussed in more detail while also being compared to transformation optics and a popular finite element method implementation of the non-local HDM.

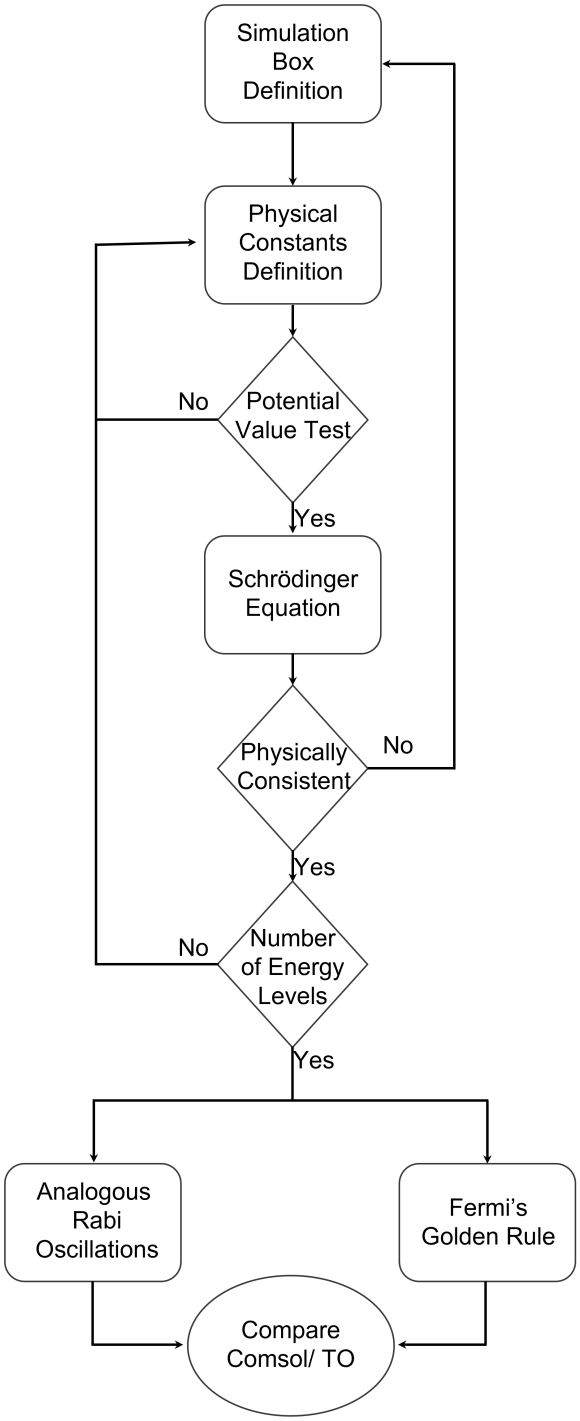

Figure 3.3 Flowchart to present the python script to solve the Madelung transformed Schrödinger equation.

Chapter 4

Results

****

Section 4.1 of this Chapter is an edited version from **Rúben A. Alves**, Ariel Guerreiro, and Miguel Navarro-Cía, *Bridging the hydrodynamic Drude model and local transformation optics theory*, Phys. Rev. B 101, 235412, 2020 [60].

****

In the previous chapters, I have explained the methodology that I developed and the transformation optics technique that I will compare my results with. In this chapter, I will show and discuss the results for both the local and non-local models.[†]

4.1 Local Models

In order to test the local limit of the Madelung formalism with the hydrodynamic Drude model, I compare the results with transformation optics. In

[†]A succinct version of this chapter can be found in [60].

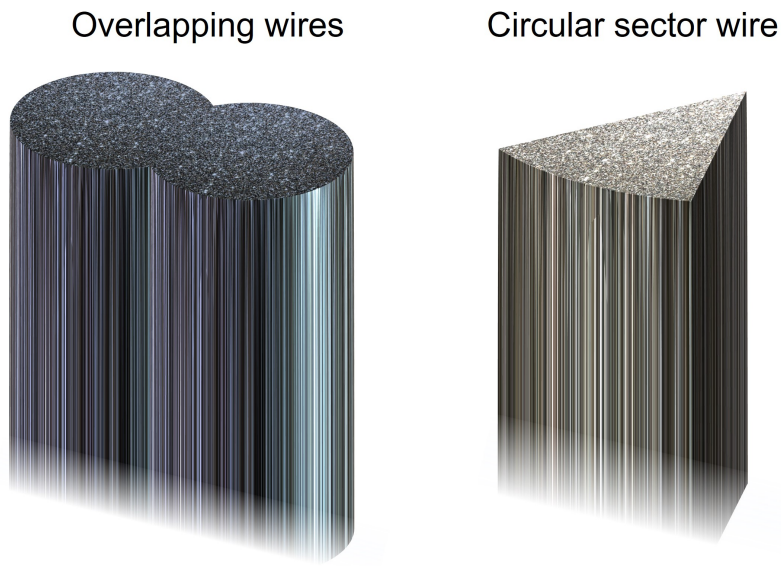

Figure 4.1 3D models of the two geometries studied.

the next section I will show how to apply transformations optics, first to the system discussed previously, the overlapping nanowires and then to the circular sector. These geometries can be seen in Fig. 4.1

4.1.1 Overlapping Nanowires

I will now discuss and present the results found for the overlapping nanowires.

The cross section of such system can be seen in Fig. 2.2.

Transformation Optics

As previously shown, the response of this system to light can be solved analytically with the assistance of transformation optics. So for now I will consider that the incident light is horizontally polarized.

Fig. 4.2 shows the cross section of the nanowires (Fig. 4.2A) and its

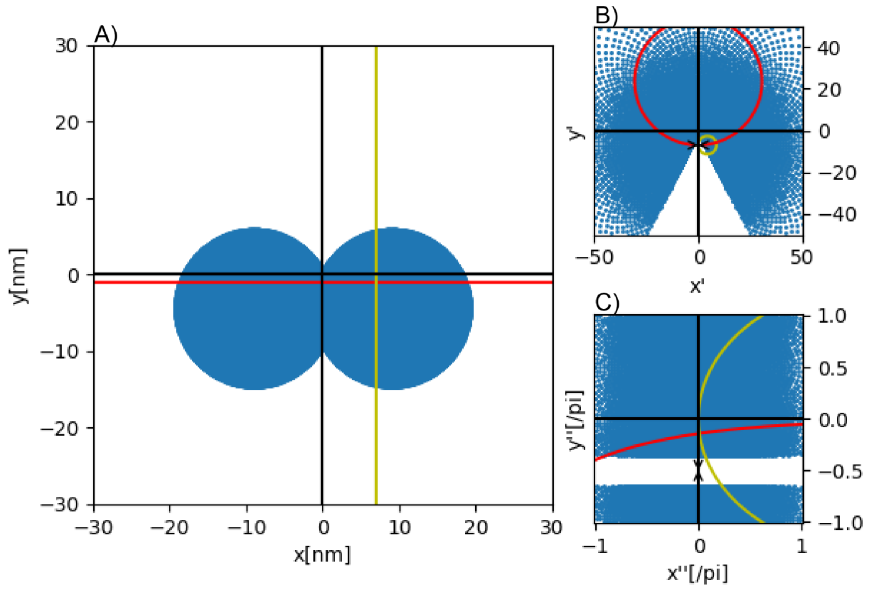

Figure 4.2 Cross section of the nanowires in the real world (A), and in the virtual world z' (B) and z'' (C). Figure taken from [60].

transformations (Fig. 4.2B and C) under the same conformal transformations shown in section 2.2. This figure was obtained using a python code that was originally given 512 points to draw Fig. 4.2A. Following the first transformation given by $z' = \frac{g^2}{z} - ir_0$, where r_0 is a constant that relates to the intensity of the electromagnetic field in the real world and the position of the dipole in the first virtual world, $z' = x' + iy'$ are the coordinates of the first virtual world and $g^2 = 2r_0\sqrt{R^2 - \frac{D^2}{4}}$, where R is the radius of a single nanowire and D is the distance between the two centres of each nanowire, the python code shows the infinite wedge-type geometry in Fig. 4.2B. Using the second transformation $z'' = \ln(\frac{z'}{r_0})$, where $z'' = x'' + y''$ are the coordinates of the second virtual world, one can finally see the infinite periodic metal-dielectric-metal slab, where in Fig. 4.2C only shows a single period. The yellow and red line represented in Fig. 4.2 are for $x = 7$ and $y = -1$, receptively. Their purpose are to add a visual aid for the transfor-

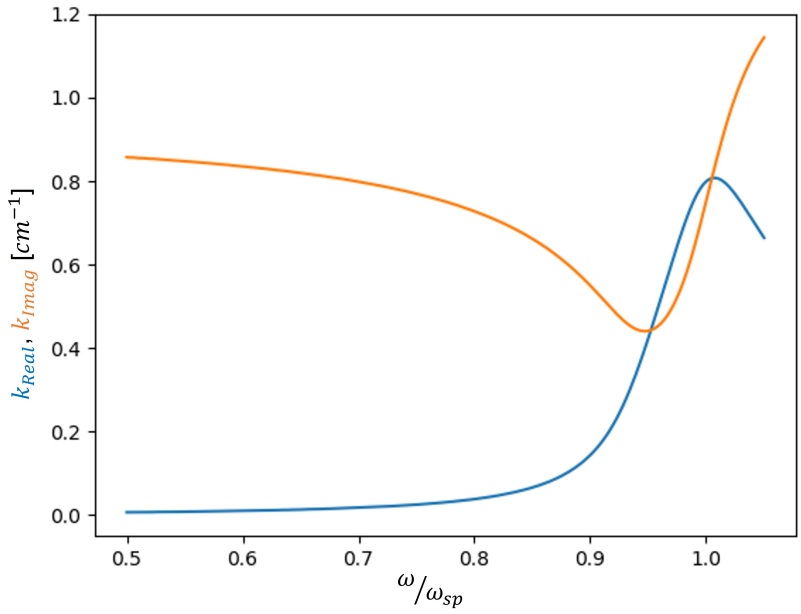

Figure 4.3 Solution of Eq. 4.1 for $D = 4\ nm$. k_{real} is represented in blue and k_{imag} in orange.

mations as with them one can visualise the transformation of the original world coordinate system.

With the conformal transformations, one can now use Eqs. 2.5 and 2.6 to have the dispersion relation of the system that is given by

$$\varepsilon \tanh(k\theta_0) = -\tanh(k(\pi - \theta_0)). \tag{4.1}$$

Eq. 4.1 is a complex transcendental equation. In order to solve this equation, I implemented a python code using a variation of the Newton's method. This code would divide Eq. 4.1 into the real part and imaginary part to solve for

$$k(\omega) = k_{real} + ik_{imaginary}. \tag{4.2}$$

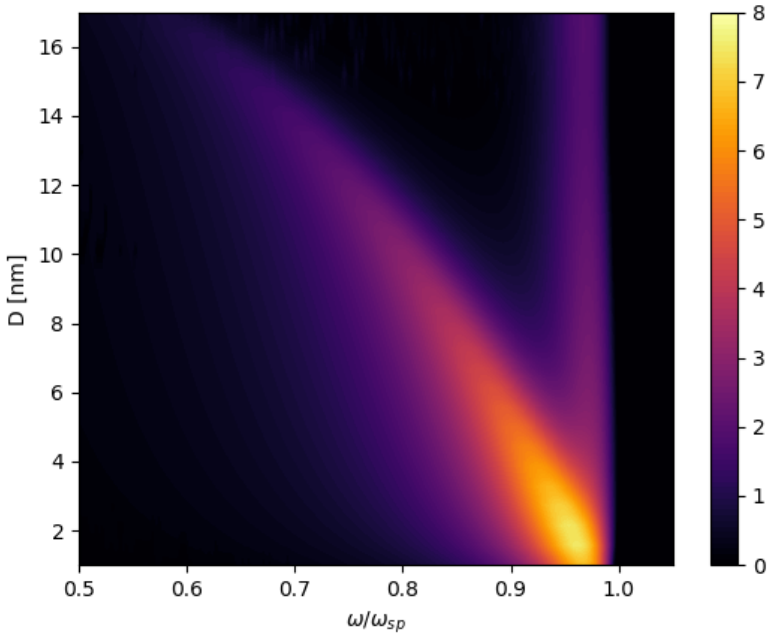

Figure 4.4 TO-computed absorption cross section spectrum of two circular overlapping $R = 10\ nm$ nanowires as a function of the distance between their centers, D. Note that the absorption cross section is normalized to the dimer axis; that is, to the horizontal dimension x, see Fig. 4.2. Figure taken from [60].

The detailed description of the python code and it inner workings can be found in Appendix A.

Fig. 4.3 shows the solution to Eq. 4.1 for $D = 4\ nm$. For each distance D considered there needs to be a corresponding solution of Eq. 4.2. With this equation solved, one can now calculate the absorption cross section of the system with

$$\sigma_a = 2\pi^2 k_0 \frac{\Sigma^2}{\theta_0} \Re(k\Gamma), \tag{4.3}$$

where $\Sigma = D\sin(\theta_0)$, $\Gamma = \frac{\varepsilon \cosh^{-1}(k\theta_0) e^{-k\theta_0}[1+\tanh(k\theta_0)]}{\varepsilon - \varepsilon_c + \varepsilon(\varepsilon\varepsilon_c - 1)\tanh^2(k\theta_0)}$ and $\varepsilon_c = \frac{\theta_0 - \pi}{\theta_0}$.

Fig. 4.4 shows the solution of Eq. 4.3. Even though TO has been widely

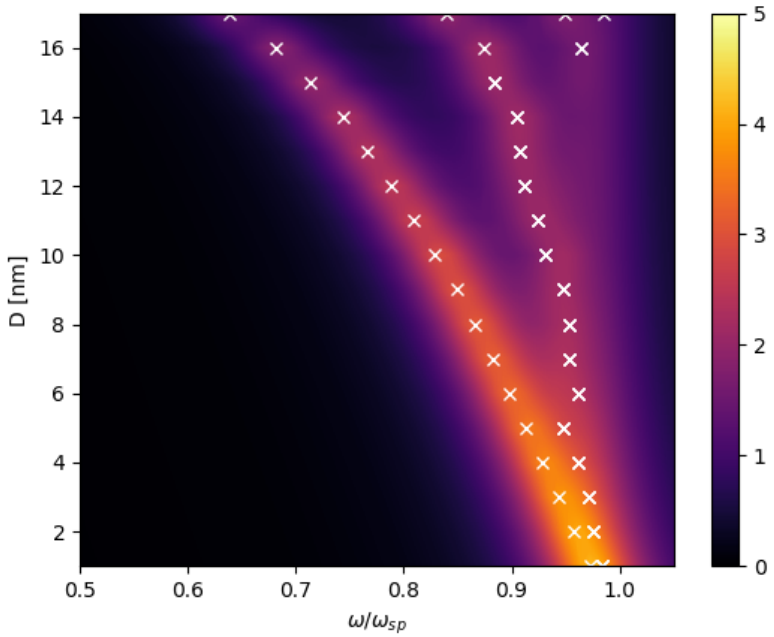

Figure 4.5 Comsol-computed absorption cross section spectrum of two circular overlapping $R = 10\ nm$ nanowires as a function of the distance between their centers, D. Note that the absorption cross section is normalized to the dimer axis; that is, to the horizontal dimension x, see Fig. 4.2. The white crosses represent the eigenfrequencies of the system. Edited version from [60].

used successfully in the field, I have compared its solutions to a full-wave solution using COMSOL shown in Fig. 4.5; the details of the simulation can be found in the Appendix B. One should note that Madelung assumes a propagation along the infinite axis of the geometry, while the absorption cross section shown here assumes a propagation in plane. This mismatch could be a source of error. However, I would like to propose an hypotheses that the most important factor is the direction of the polarization. In order to test this hypothesis, I have prepared a Comsol script that calculates the eigenmodes of the system. This script assumes a propagation out of plane and its solutions are marked with the white crosses in Fig. 4.5. As one can see, the eigenmodes are consistent with the absorption peaks of the system which validates the previous hypothesis.

By comparing Fig. 4.4 with Fig. 4.5, one can notice that the first plasmonic mode from the COMSOL simulation matches directly with the one obtained using TO. One should note as well that even though the model is able to capture higher order modes if the plasmonic system is illuminated by a nano-emitter [75, 76, 97–99], this is not the case if the excitation is done by a plane wave.

Madelung Formalism

Now that the one has the absorption cross section calculated with transformations optics, I can now show the results using the Madelung formalism in association with the HDM. In order to push this model to the utmost local limit, I have linearised the Schrödinger equation and by defining the linear potential with a sharp interface between the metal and the surrounding environment. The value of the potential was chosen to be such that it allows to have at least 5 different bound energy states (I will show later the need to

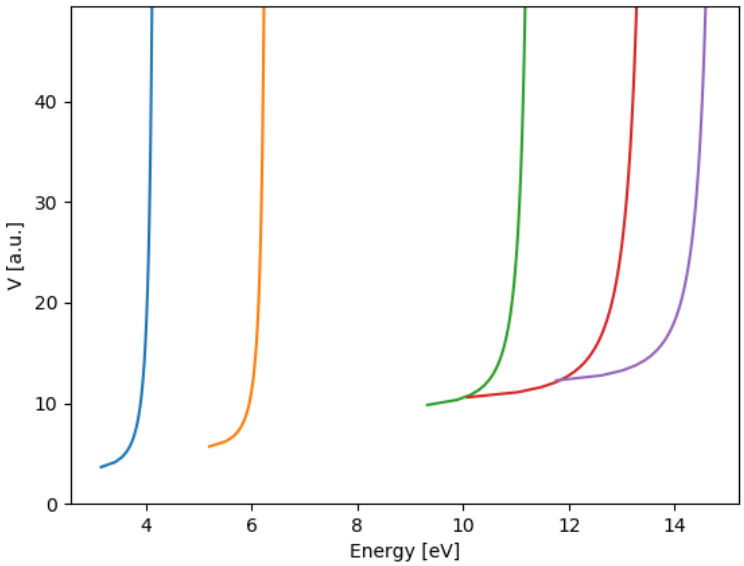

Figure 4.6 Energy values of the first five energy level and their dependence to the values of the potential for $D = 15\ nm$.

choose a wise number of eigenstates considered, to capture the underlying physics while avoiding non-physical artefacts). In order to do this study, I have solved the Schrödinger equation for different values of V for a system with a distance $D = 15\ nm$.

Fig. 4.6 shows the dependence of the energy values of the system to the value of the potential. In this thesis, the value chosen was 45. This value ascertains that the five-energy levels considered are already in the asymptotic regime and thus are not affected by this choice. This asymptotic regime is reached when the value of the potential is so high that it can be considered as infinite. Although not in the scope of this thesis, there could be a way to define this value by employing a Jellium model to the metal and determine the effective value of this potential. This is left as a possible future work.

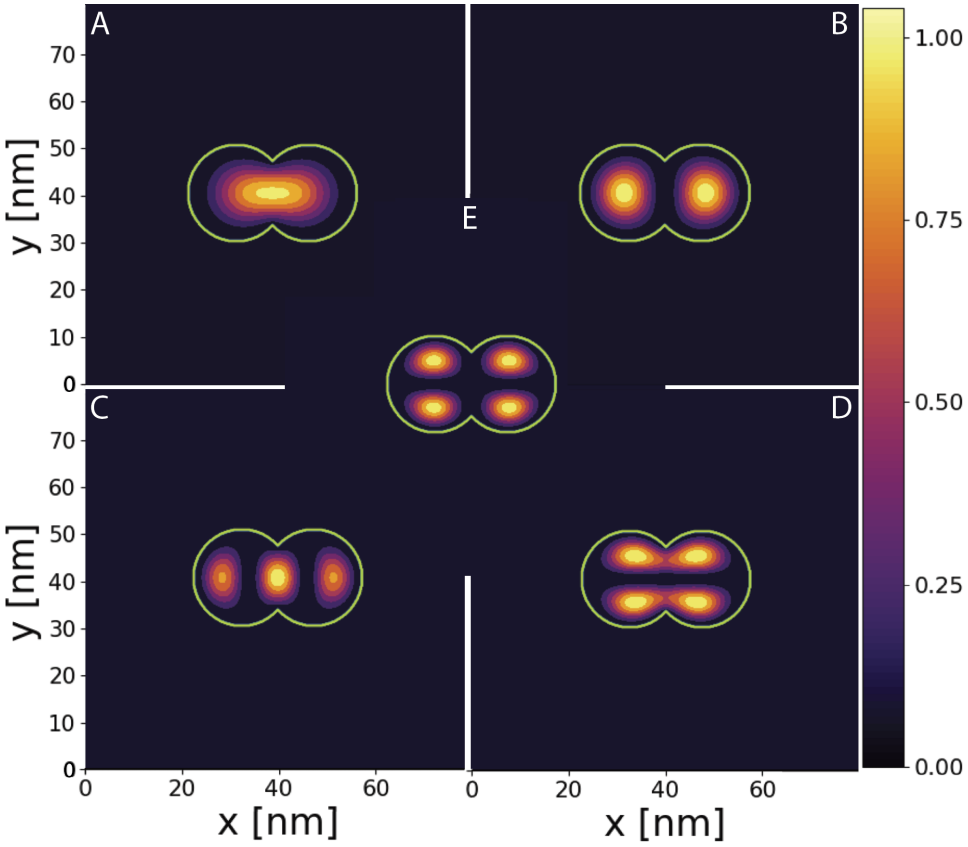

Figure 4.7 Normalized electron density distribution corresponding to the first five eigenstates (A-E) of two overlapping nanowires for $D = 15\ nm$. Figure taken from [60].

With the value of the potential determined, one can now solve the Schrödinger equation.

Fig. 4.7 shows the solutions of the linearised the Schrödinger equation where the potential $\mathcal{U}$, defined in Eq.3.34, has the profile represented in Fig. 3.2A. This implies that the metal interface vanishes abruptly which is not physically possible. However, with this consideration, one can push the model to its local limit. Later in this chapter, I will consider super-Gaussians instead of a step functions to describe the potential $\mathcal{U}$ in order to capture one non-local effect, the electron spill-out. Due to the modularity of

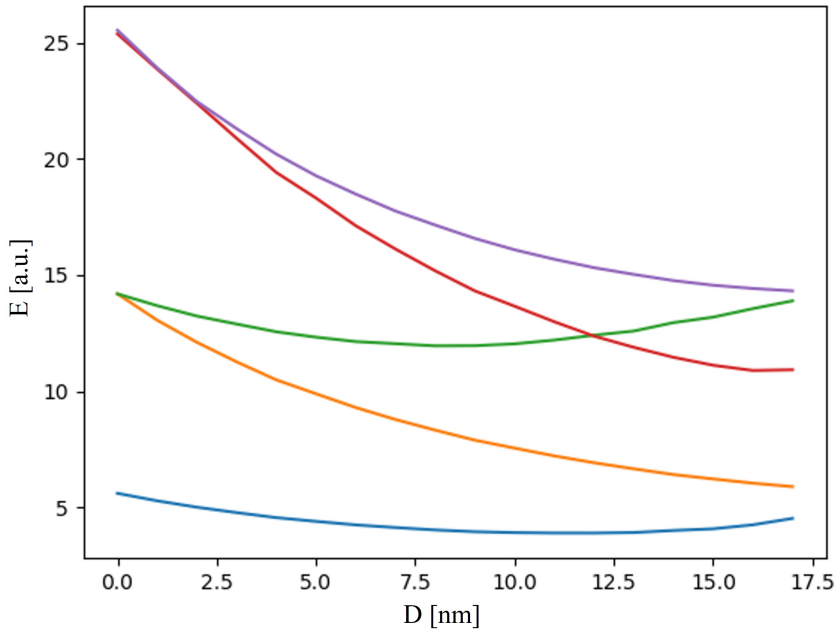

Figure 4.8 First five energy levels of the system as a function of the distance D. Figure taken from [60].

this model, one can introduce these effects one by one in order to eventually reach a full non-local description of the system. The solutions represented in Fig. 4.7 were found using a python script that used the finite difference method. This script is briefly explained in Appendix A.

A full parametric study was done and the evolution of the energy levels for each D can be seen in Fig 4.8. With these results, one can calculate the probability of a transition between energy levels with the Rabi oscillations. In practice, the plasmonic structure acts as a small antenna which absorbs and re-emits light. Given the total size of the overlapping nanowires, scattering can be neglected. Therefore, the absorption cross section should be proportional to $|C_b(t)|^2$ from Eq. 3.43 in a two-level system. As one increases the distance D, up to the limit of 20 nm, the energy levels start to

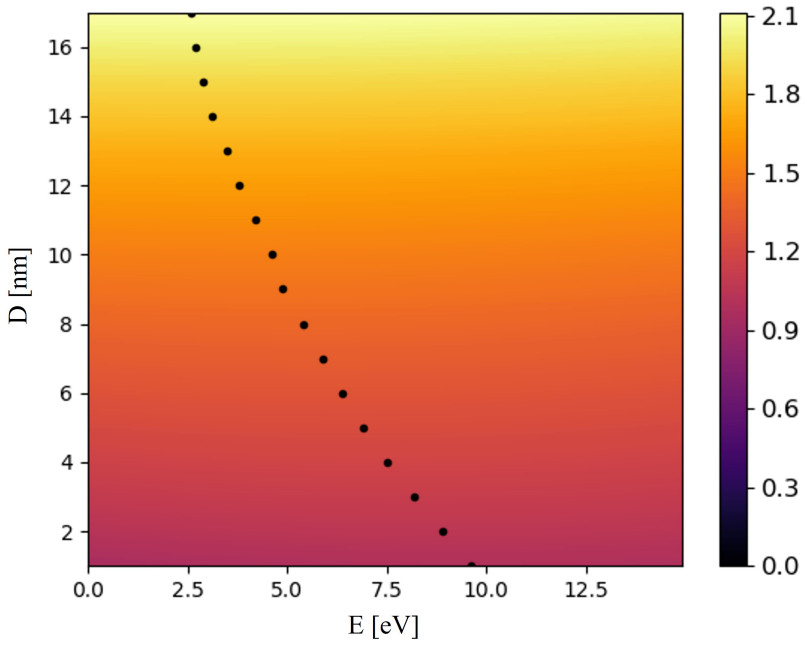

Figure 4.9 Sum of all the Rabi coefficients for a five-level system. Notice that the black dots represent the maximum of the sum and that the $x-$axis is the energy of the incident light. Figure taken from [60].

drift back to their initial position. Once one reaches the 20 nm limit, instead of having two overlapping nanowires, one has two isolated nanowires. We should also note the crossing of the third and fourth energy levels at around $D = 12\ nm$ in Fig. 4.8. This is the due to the shift of energy of these two eigenstates (Fig. 4.8c,d) being so large as a function of D, that the actually cross between each other.

Fig. 4.9 shows the linear combination of all the Rabi coefficients for a five level system as a function of the distance D and the energy of light defined in eV. One can do this by solving Eq. 3.43 for every combination possible between the five levels considered. One should also remember that the solution of the Schrödinger equation described in the Madelung formal-

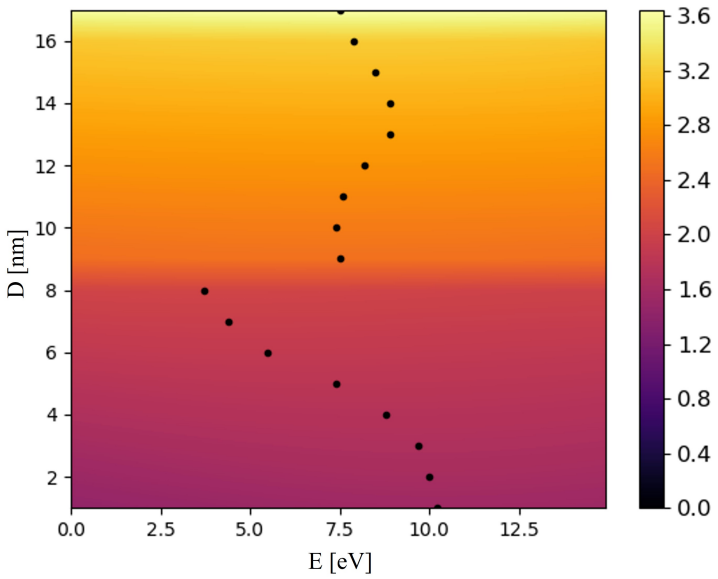

Figure 4.10 Sum of all the Rabi coefficients for a seven level system. The black dots represent its maximum.

ism is a linear combination of all of the eigenstates. Since it is impossible to compute all of the states, as there are an arbitrarily large amount of them for large potential wells (for a infinite potential there is an infinite amount of eigenstates), one needs to find the correct truncation in the number of eigenstates to achieve convergence. In our case, 5 eigenstates provide good results. Perhaps counter-intuitively, in the methodology presented here, increasing the number of eigenstates does not necessarily lead to more accurate results. Indeed, it can lead to non-physical artefacts. To illustrate this, Fig. 4.10 is the equivalent to Fig. 4.9 but when considering 7 eigenstates. The jumps experienced by the dots are not physical. In order to explain this one needs to look at the behaviour of the seven energy levels as a function of the distance D.

In Fig. 4.11, the energy of the first seven levels are depicted. If one orders

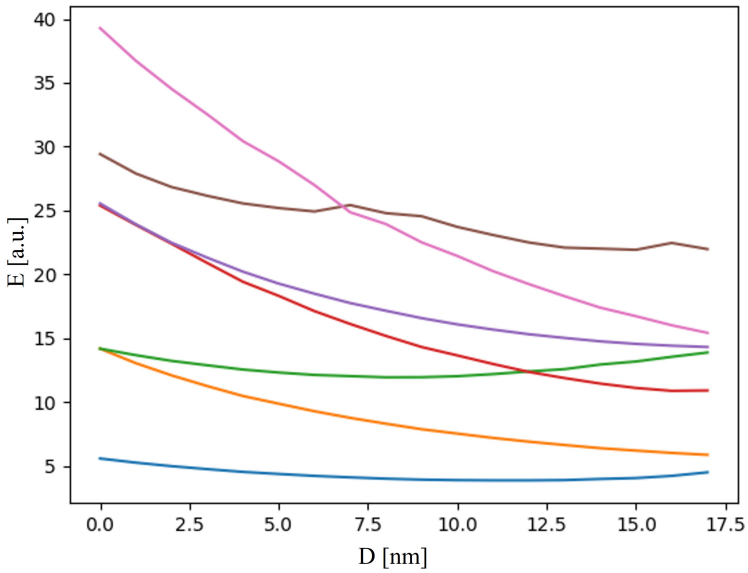

Figure 4.11 First seven energy levels for two overlapping circular nanowires

the energy levels when the system is just one wire ($D = 0$), by looking at the sixth level (in brown), one can see that what my algorithm considers one energy level is actually composed of several different incomplete energy levels. This is due to the fact that the algorithm orders the energy levels by their energy value. This means that to complete the sixth level in full in the range of D considered here, one would need to compute all the levels that it crosses with. If these new levels would, in turn, be crossed with other higher levels; then I would be forced to compute them as well. Forcing me to calculate more and more energy levels in an endless loop. This means that the choice of number of energy levels to compute has to fall into a sweet spot. On one hand, the more energy levels one computes, the more accurate a solution is. On the other, all the levels computed can only cross with each other and not with one outside of the computation. In order to test this

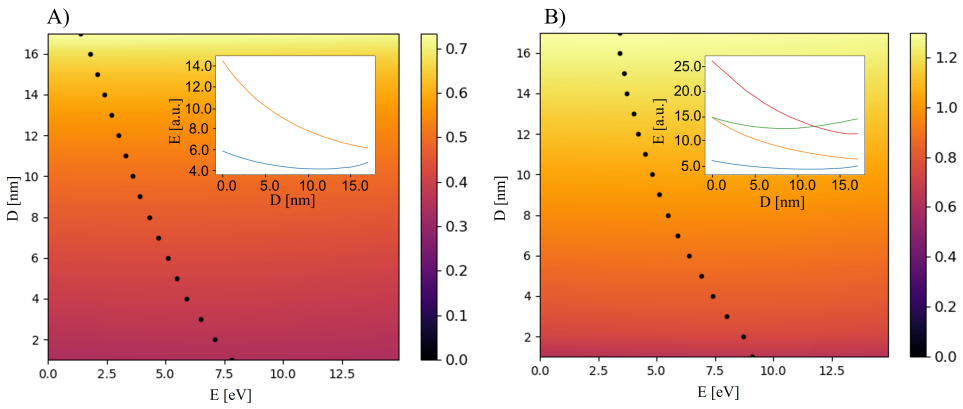

Figure 4.12 Linear combination for all the Rabi coefficients for a two (A) and four (B) level system. Dots represent the maximum. Insets: corresponding energy levels as a function of D.

hypotheses, I have also computed the Rabi coefficients when considering 2 and 4 energy levels. Fig. 4.12 illustrates that in the absence of eigenstates crossings (as the case of only the first two energy levels) or the crossing is fully encapsulated (such as the case for third and fourth energy levels crossing shown in the inset of Fig. 4.12B) the Rabi coefficients behave as expected. However, the slight blue-shift at lower values of D and the red-shift at higher values of D when compared to the five level system clearly show the need to consider more eigenstates for accurate results.

Discussion (Edited version from [60])

Fig. 4.13 shows the fitting parameter between the two models. This fitting parameter is calculated with the ratio of the energy of light where the absorption cross section reaches its maximum obtained with TO and the energy of the maximum of the Rabi oscillations. The maximum of the coefficients of the Rabi oscillations represent the maximum probability of absorbing a photon that results into a state transition. This fitting parameter can then

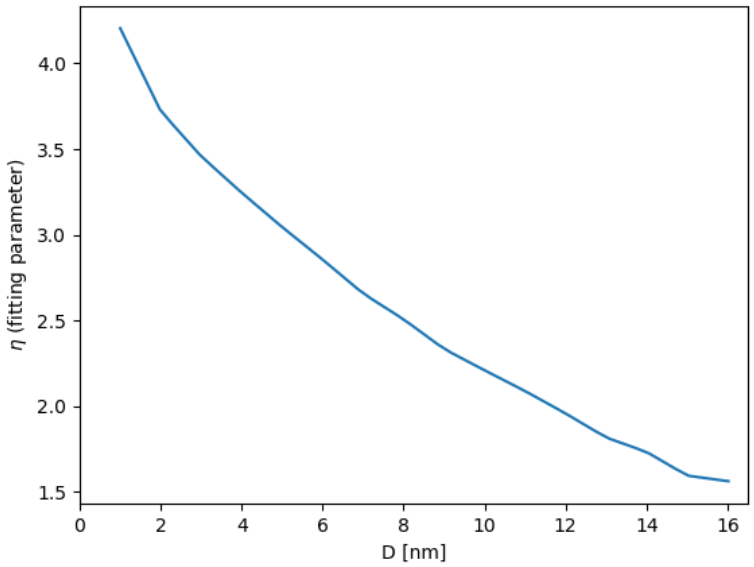

Figure 4.13 Fitting parameter between both models presented as a function of D. Figure taken from [60].

be calculated for each value of D. When both nanowires overlap considerably (i.e. small values of D), the higher-order modes emerge close to the fundamental mode. This influences greatly the latter. For larger values of D, even if the number of these higher-order modes to be considered is greater, their influence, however, is decreased significantly. This is because of the large red-shift of the fundamental mode compared to the higher order modes. This means that the ratio shown in Fig. 4.13 decreases as a function of D. In addition, the effects of non-locality are known to decrease for larger structures, making the results of the Madelung formalism and HDM more comparable with the local TO. Notwithstanding, this ratio is not linear. This can only mean that solving only the linear potentials of the Schrödinger equation does not completely result into the local limit of the HDM. Which means that the linearized Madelung formalism still, at

least, partially retains non-local effects. However, this result still provides the groundwork to implement a non-local potential which is discussed next.

4.2 Non-Local Models

The Madelung formalism with the HDM and the original hydrodynamic Drude model are inherently non-local models. Depending on the conditions that one applies to the equations; the HDM as found in the literature introduces non-local effects with specific boundary conditions and the Madelung formalism can introduce non-local effects in the potential to be solved in the Schrödinger equation. Here, I will introduce a non-local effect named electron spill-out with the introduction of a potential defined with super-Gaussians. In the literature, several approaches have been considered to deal with the HDM for the electromagnetic non-local response of plasmonics systems [100]. This thesis uses the popular COMSOL Multiphysics® implementation of the HDM [101] and assume it as the ground truth for comparison purposes. This implementation is explained in more detail in Appendix C.

4.2.1 Circular Sector

In this section, I will discuss and present the results for the circular sector. A $3D$ model of the geometry can be seen in Fig. 4.1(right).

Madelung Formalims

In order to capture the non-local effect electron spill-out with the Madelung formalism, I have described the potential on equation Eq. 3.34 with super-Gaussians.

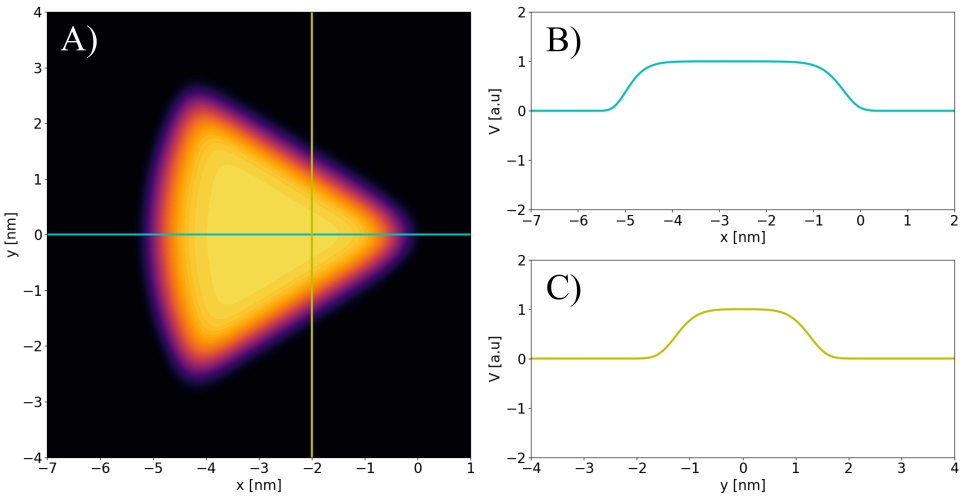

Figure 4.14 A) Representation of the potential used to describe the circular sector. B) Representation of the potential at $y = 0$ section shown in cyan in the panel A. C) Representation of the potential at $x = -2$ section shown in yellow in the panel A.

The representation of the potential defined with the super-Guassians is shown in Fig. 4.14. This super-Gaussian is a circular sector or wedge that follows the following equation.

$$\mathcal{U}(x, y) = U_0 exp\left(-\frac{(x - x_0)^2}{2\sigma^2} - \frac{(y - y_0)^2}{2\sigma^2}\right)^p, \tag{4.4}$$

where $\sigma = 1$, and p, the sharpness of the super-Gaussian, is arbitrarily set to 10 to have a high roll-off akin to the literature [102–104]. U_0 is the value of the maximum of the potential ($U_0 = 1$ in Fig 4.14) and $x_0 = 0$ and $y_0 = 0$ define its centre with a radius of 5 nm.

The potential at $y = 0$ (that is, along the horizontal cyan line on the left hand side of Fig. 4.14) is shown clearly on the top right corner of Fig. 4.14 to show how the super-Gaussian is drawn, idem for the potential at $x = 0$ on the bottom right corner. As it is observed, the profile follows a step-like

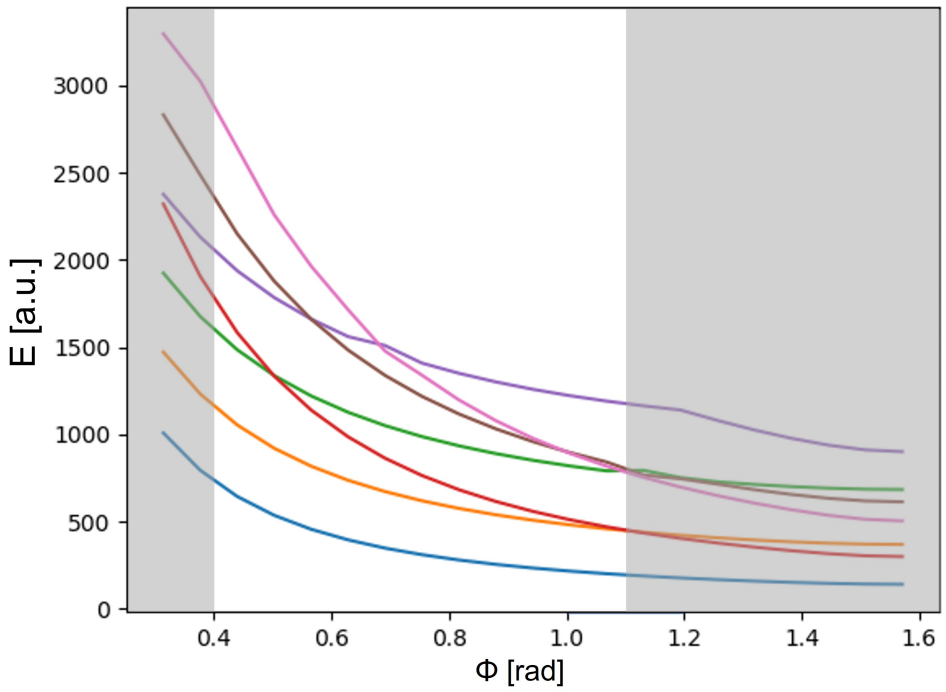

Figure 4.15 First seven energy levels of the geometry defined as a function of the circular sector central angle ϕ, where each colour represents a different state. The clear zone represents the truncated parameter sweep.

function. However, note that the edges are not sharp as the super-Gaussian function makes the boundary between metal and background (assumed to be air for our COMSOL Multiphysics® simulations) smooth. By doing this, I can mimic a more realistic structure as at the nanoscale, the boundary of the metal system would not be well defined while it also allows for the electrons to "leave" the metallic system and then be pushed back.

With the potential well defined, I can now solve the Schrödinger equation. In order to obtain a proxy for the macroscopic absorption cross-section property based on the Fermi's golden rule as described previously, we linearised Eq. 3.34 as a first order approximation.

Fig. 4.15 shows the energy levels of the states of the linearised Schrödinger equation as a function of the central angle of the circular sector ϕ. Comparing these solutions to the ones found in Fig. 4.8, one can already see that the number of crossings are much greater. This brings an unforeseeable problem. As discussed previously, in order to obtain the most trustworthy results one should compute a number of energy levels that cross only with each other. Otherwise, behaviour seen in Fig. 4.10 can be misunderstood. Because the number of crossings is much greater in the circular sector, instead of increasing and/or decreasing the number of energy levels calculated, one can restrict the parametric sweep to a self-contained range. If one considers only the sweep between $0.4rad$ and $1.1rad$ (the non-grayed area in Fig. 4.15), then all crossings happen between each of the energy levels considered without the interference of the ones not computed. Notice that for $\phi < 0.4rad$ there an incomplete crossing in the seven energy level in pink (as before, I am ordering the energy levels first for lower values of ϕ and then preserving it), whereas for $\phi \geq 1.2rad$ there is another incomplete crossing, this time in the fifth energy level in purple. It is also worth to point out that the small inflection of the fifth energy level, in purple, at $\phi \approx 0.7rad$ is due to unavoidable computational error and not an actual crossing with a different energy level.

After solving the Schrödinger equation, one has everything needed to solve Eq. 3.48. This solution can be found in Fig. 4.16. One should note that the energy values encountered in the $x-axis$ come from the interaction Hamiltonian H_I making it possible for us to find the resonances of the system. The dots represent the maximum of the absorption cross-section that correlates to the first plasmonic mode of the system. Due to the number of energy levels computed, it also possible to see the second plasmonic mode

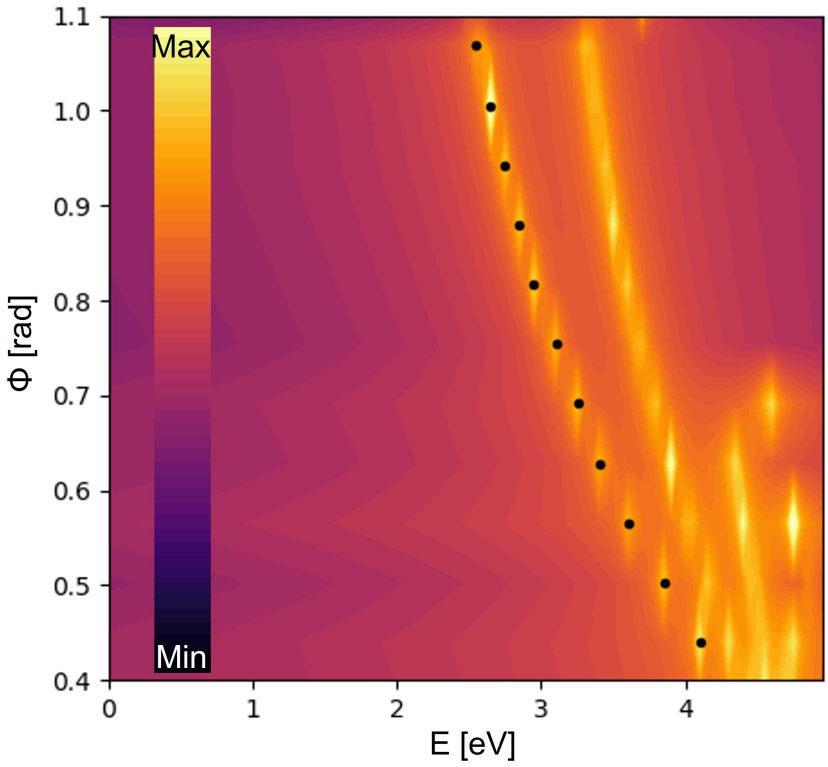

Figure 4.16 Proxy for absorption cross-section calculated from Eq. 3.48, using the first seven modes in log scale. The dots represent the maximum value of the absorption. The energy values on the $x - axis$ are the energy of light considered.

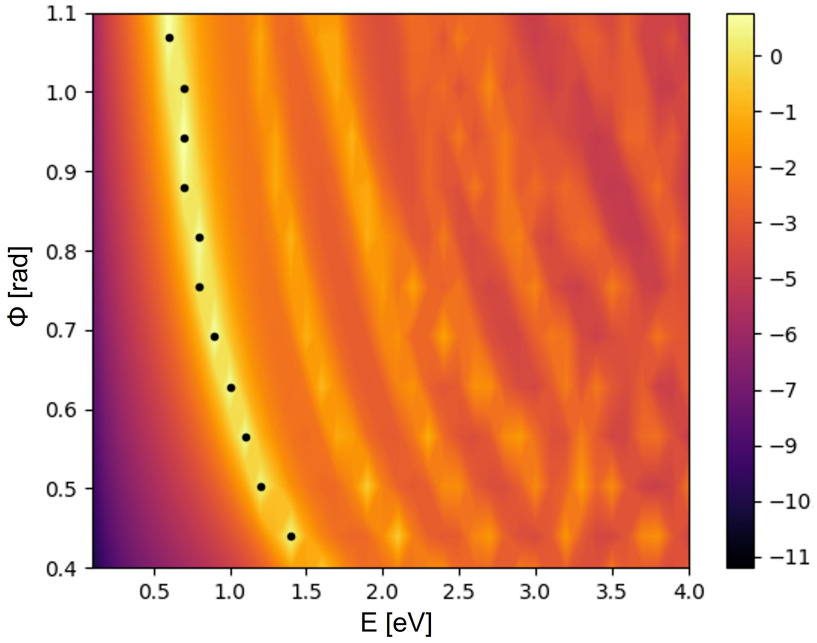

Figure 4.17 Non-local absorption cross-section in log scale calculated using the popular hydrodynamic model finite-element implementation by *Toscano et al.* [101] normalized to the area of the cross section.

of the system. However, all comparisons with the model implemented in COMSOL Multiphysics® simulations are done only considering the first mode.

In order to compare, and validate, these results, I solved the same geometry using the popular COMSOL Multiphysics® implementation of the HDM [101] (see Fig 4.17).

The first property visible in both models is that by increasing the angle ϕ, the energy of the resonance decreases, which could be found counter-intuitive from previous local studies of bowties [76, 97, 105]. However, this is where transformation optics can shine.

Transformation optics can be enormously restrictive when applied to

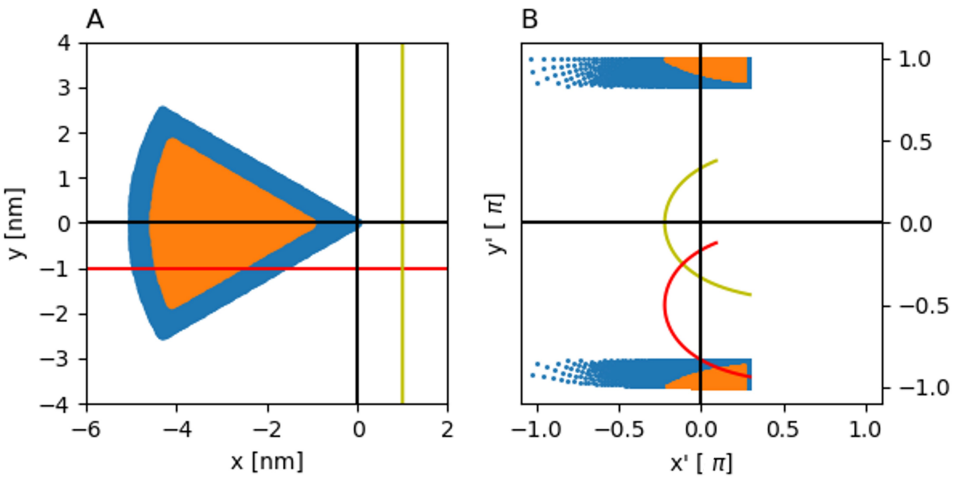

Figure 4.18 Schematic of the geometry and its virtual space after transformation optics.

non-local models. Most of the models formulated to include non-localities do so by creating a virtual dielectric layer between the bulk metal and the background. This means that aside from a very specific set of geometries, this layer will be transformed in the virtual world in such a way that will prevent one to solve the system analytically. Even so, if one applies the transformation to the geometry, then transformation optics provides enough physical insight that one can understand this counter-intuitive behaviour of this system.

Fig. 4.18A shows the schematic of the circular sector with the layer (in blue) between the bulk metal (in orange) and the background (in white). The red and yellow lines are visual aids of the transformation. Fig 4.18B shows the same geometry under the conformal transformation $z' = ln(z)$. Although this periodic heterostructure cannot be solved analytically, it can explain the red shift due to the impact of the non-localities. In the transformed space, what was once only a dielectric shell engulfing the metallic domain, now, it takes the majority of the are in one period. The metallic

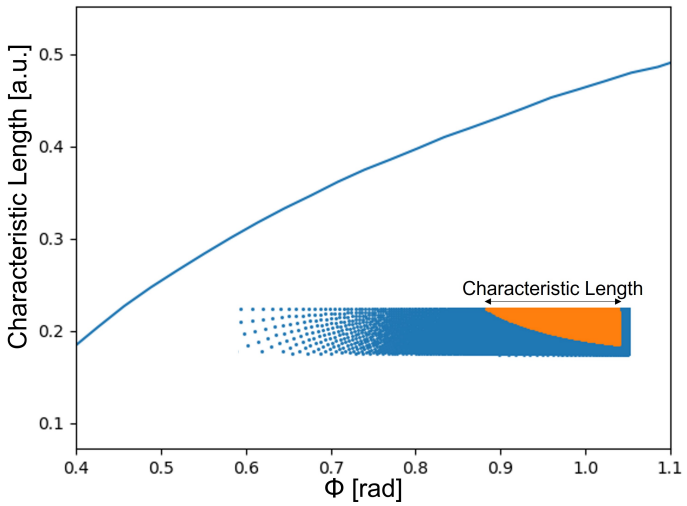

Figure 4.19 Relationship between the characteristic length of the nanoparticle-like structure in the virtual space (that is, the horizontal length of the bulk metal) and ϕ.

domain in the virtual space is all but squeezed out into a nanoparticle-like structure. This means that instead of having a periodic metal-insulator-metal structure that one finds in the local case, this new geometry resembles more an array of nanoparticles embedded in a non-homogeneous dielectric environment. This situation is exacerbated due to the non-linear relationship with the central angle of the circular sector and the size of this virtual nanoparticle-like array as shown in 4.19. This explains the red shift, just like a nanoparticle, with the increase of ϕ (so, increase of particle size in the virtual world) for the non-local case instead of the blue shift found in the local case for circular sectors and bowties.

Getting back to Fig. 4.16, the other feature that is noteworthy is the fact that at lower values of ϕ, the resonances are closer to the plasma frequency. This increases the interactions of different modes which makes it difficult to distinguish between the first mode (marked by the dots on the figure) and

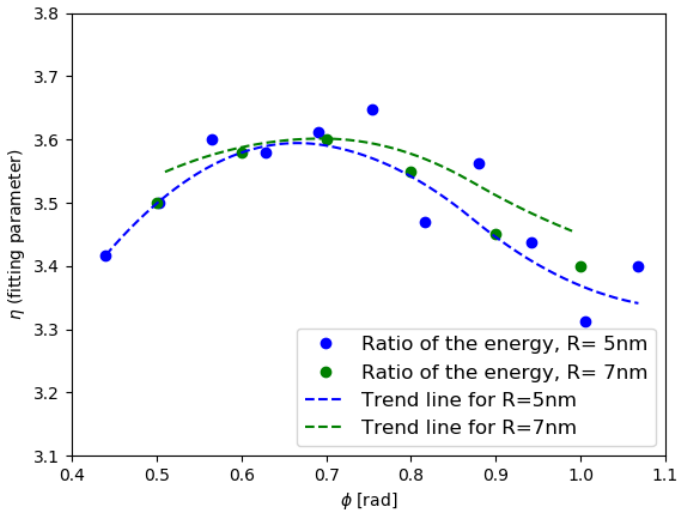

Figure 4.20 Fitting parameter as a function of D.

the higher order modes. This is not visible in Fig. 4.17 due to the distinction of the virtual dielectric shell and the bulk metal. In Fig. 4.17, it is worth mentioning as well that for higher values of ϕ, some dots that mark the first mode appear to be vertically aligned. This is due to a computational error and the lack of computational resources. In order to address this problem, one would need to use a finer mesh that would increase the computational time past the acceptable and practical value.

Discussion

Fig. 4.20 shows the ratio of the energy of the absorption cross section maximum obtained with *Toscano et al.* [101] implementation and the energy of the maximum of the Fermi's golden rule (i.e. the maximum probability of absorbing a photon that results into a state transition) obtained with the Madelung HDM for each value of circular sector angle ϕ.

Figure 4.20 shows that η is more stable when compared to the previous

local case, as its absolute value is of a smaller interval raging from 3.30 to 3.65. This is to be expected with the application of super-Gaussians to define the geometry. With these types of potentials the linearised Madelung methodology starts capturing non-local effects (namely electron spill-out). The fact that this ratio is not constant at the value 1 means that the non-linear terms in the potential that were not considered still retain some non-locality, however small.

In order to stress test the model presented here, I have also computed a small parametric run of a slightly altered geometry. Represented in green in Fig. 4.20, is the same η for a circular sector with radius $R = 7\ nm$. As one can see in the figure, aside from computational errors, both models react to the change in a very similar way, thus proving that once this η is found for one geometry it will be invariant to small changes.

Chapter 5

Conclusions and Future Work

This thesis presents different approaches to modelling plasmonic systems. It starts showing that transformations optics can be used as a powerful technique to analytically describe plasmons. It also shows that even when transformations optics cannot be used to solve analytically the problem, due to its drawbacks, it still provides physical insight and intuition that other tools and techniques might lack. In this thesis, I have shown the advantages and limitations that this technique has.

The main objective of this thesis was to present a new methodology to the semi-classical model of the hydrodynamic Drude model. By associating it with the Madelung formalism, I have shown how one can reshape the fluid equations into a non-linear Schrödinger equation and use methods commonly found in quantum optics to solve the equation and obtain the response of the system to the electromagnetic field without having to define additional boundary conditions. Also, in this thesis, it is shown that by using the Madelung formalism one can organise the problem into modules

and introduce step-by-step each of them into the equations. First, I stress test the model into the local limit and compare it with full wave simulations and transformation optics. By doing so, I was able to understand the effects of the choice of number of energy levels computed that then could be carried over to the non-local model. By describing the geometry of the system with a potential, one not only has complete freedom on its shape but can also introduce non-local effects such as electron spill-out using super-Gaussians. All of the results were compared to full wave simulation and were tested to ensure their validity.

One of the major advantage of the model being modular is that there is always room to grow. Just to give my opinion on which ones should take priority; Instead of using an analogous to the Fermi's golden rule to obtain a proxy to the microscopic absorption cross section, one could instead introduce it with the Gorini–Kossakowski–Sudarshan–Lindblad equation (GKSL equation) also know as the master equation $\dot{\rho} = i\hbar[H, \rho] + \mathcal{L}$, where $\mathcal{L}$ are the Lindblad terms. With this, one could use the Lindblad terms to introduce the ohmic losses into the system, however at the cost of the hermiticity of the equation. One other possible venue to improve this model, is to describe the potential in the Schrödinger equation not with an arbitrary value but in association with a Jellium model. With it one could arrive at a potential that would describe a real metal instead of an ideal one. Last but not least, I also think that solving the full non-linear Schrödinger equation instead of linearising it could also provide some merit. This is only three of the many examples where the model could be improved.

Chapter 6

Scientific Outputs with Author's Contribution Statement

The work carried out during the PhD has been disseminated as follows:

1. Peer-reviewed scientific articles

   Rúben A. Alves, Victor Pacheco-Peña, and Miguel Navarro-Cía, *Madelung formalism for electron spill-out in non-local nanoplasmonics*, under review.

   Author's contribution: I performed the Madelung-based numerical calculations and Comsol simulations, processed and analyzed the data and wrote the first draft of the manuscript.

   Rúben A. Alves, Ariel Guerreiro, and Miguel Navarro-Cía, *Bridging the hydrodynamic Drude model and local transformation optics theory*, Phys. Rev. B 101, 235412, 2020 [60].

Author's contribution: I performed the Madelung-based numerical calculations, conformal transformation analysis and Comsol simulations, processed and analyzed the data and wrote the first draft of the manuscript.

Victor Pacheco-Peña, **Rúben A. Alves** and Miguel Navarro-Cía, *From symmetric to asymmetric bowtie nanoantennas: electrostatic conformal mapping perspective*, Nanophotonics, vol. 9, no. 5, 2020, pp. 1177-1187, 2020 [76].

Author's contribution: I contributed to the discussion and the writing up of the manuscript.

Victor Pacheco-Peña, **Rúben A. Alves** and Miguel Navarro-Cía, *Hidden Symmetries in Bowtie Nanocavities and Diabolo Nanoantennas*, ACS Photonics 2019 6 (8), 2014-2024, 2019 [75].

Author's contribution: I contributed to the discussion and the writing up of the manuscript.

2. Conference contributions

Rúben A. Alves, Ariel Guerreiro, and Miguel Navarro-Cía, "Harmonising Nonlocal and Local Formalism for Overlapping Plasmonic Nanowires," 14th International Congress on Artificial Materials for Novel Wave Phenomena, Metamaterials'2020, New York, U.S.A., September – October (2020)

Rúben A. Alves. Ariel Guerreiro, and Miguel Navarro-Cía, "Harmonising the Nonlocal Hydrodynamic Drude Model with the Local Transformation Optics Model," Photon 2020, September (2020)

Víctor Pacheco-Peña, **Rúben Alves**, and Miguel Navarro-Cía, "Plasmonic nanoantennas and nanocavities: a transformation electro-

magnetic perspective," URSI GASS 2020, Rome, Italy, August – September (2020)

Víctor Pacheco-Peña, **Rúben Alves**, and Miguel Navarro-Cía, "Conformal transformation in bowtie nanoantennas and nanocavities: unveiling hidden symmetries," The 13th International Congress on Advanced Electromagnetic Materials in Microwaves and Optics, Metamaterials'2019, Rome, Italy, September (2019)

Víctor Pacheco-Peña, **Rúben Alves**, and Miguel Navarro-Cía, "Impact of plasmonic bowtie nanoantennas and nanocavities on the dynamics of nearby nanoemitters," META'19, Lisbon, Portugal, July (2019) - INVITED

Víctor Pacheco-Peña, **Rúben A. Alves**, and Miguel Navarro-Cia, "Self-induced trapping of quantum dots in nanocavities," Photon 2018, Birmingham, UK, September (2018)

Appendix A

Numerical Algorithms

A.1 Transformation optics and the characteristic equation

In order to find the complex roots of the transcendental equation Eq. 4.1, I have divided the equation into real and imaginary part. This was achieved by dividing the right hand side of the equation by the right hand side which leads to

$$-\frac{\varepsilon \tanh(k\theta_0)}{\tanh(k(\pi-\theta_0))} = 1 + 0i. \tag{A.1}$$

which implies that

$$\Re\left\{-\frac{\varepsilon \tanh(k\theta_0)}{\tanh(k(\pi-\theta_0))}\right\} = 1. \tag{A.2}$$

and

$$\Im\left\{-\frac{\varepsilon\tanh\left(k\theta_0\right)}{\tanh\left(k(\pi-\theta_0)\right)}\right\}=0. \tag{A.3}$$

With this, one only needs to implement the improved version of the Newton's method to find the root where the initial guess is provided by previous solution, to have the results desired. This method solves Eq. A.2 and would only accept it if the solution was the solution to Eq. A.3.

A.2 Schrödinger equation and the finite differences method

Eq 3.18 can be characterized as a eigenvalue problem. These types of problems are commonly found in computational physics and there is a wide range of solutions. Of those, the finite difference method is the one that was used. This method replaces the Laplacian with the adequate finite differences.

In a two dimensional system, a function can be represented by its values over a square grid with finite size, as represented in Fig. A.1. For the local simulations, the grid's length was 160 nm, for a number of points of 1024 and a distance between points of 0.15625 nm. For the non-local simulations, the grid's length was 25 nm, for a number of points of 1024 and a distance between points of 0.0244140625 nm.

Then, the evaluation of the Laplacian at the point (i,j) is given by

$$\Delta\psi_{i,j}\approx\frac{\psi_{i+1,j}+\psi_{i-1,j}+\psi_{i,j+1}+\psi_{i,j-1}-4\psi_{i,j}}{\hbar^2}. \tag{A.4}$$

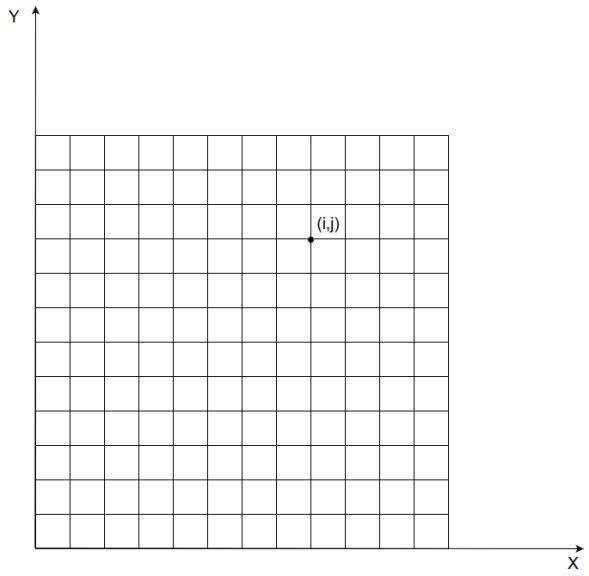

Figure A.1 Schamtic of a grid where one can numerically express the wavefunction.

This, can be expressed in matrix form, such that

$$\nabla \begin{pmatrix} \psi_{0,0} \\ \psi_{0,1} \\ \psi_{0,2} \\ \dots \\ \psi_{N,N} \end{pmatrix} = \mathbf{M} \begin{pmatrix} \psi_{0,0} \\ \psi_{0,1} \\ \psi_{0,2} \\ \dots \\ \psi_{N,N} \end{pmatrix} \tag{A.5}$$

So numerically Eq. 3.18 can be written as

$$\varepsilon x = \mathbf{A} x \tag{A.6}$$

with $x = \begin{pmatrix} \psi_{0,0} \\ ... \\ \psi_{N,N} \end{pmatrix}$, $A_{i,j} = -\frac{\hbar^2}{2m} M_{i,j} + V_{i,j}$ and $V_{i,j} = V(r_{i,j})$. This is a simple algebraic eigenproblem equation can be solved numerically using sparse matrices as provided by *Python* native module *scipy.sparse*.

Appendix B

Comsol Simulations Details

The table presents the Comsol simulations details for all the local and non-local runs.

For this thesis, the metal properties used in the Comsol simulations are from an ideal metal whose concentration of free electrons per unit of volume is 1.07×10^{28} and a dielectric permitivity of

$$\varepsilon = 1 - \frac{\omega_p^2}{\omega^2 + i\gamma\omega}, \tag{B.1}$$

where $\omega_p = 5.83563 \times 10^{15} rad/s$, $\gamma = 2.861364884 \times 10^{14} rad/s$. For Comsol implementation from *Toscano et al.*, the $\Delta d = 0.5\ nm$ and permittivity of the dielectric layer is given by the condition explained in Appendix C.

	Simulation Box Size	Boundary Conditions	Mesh		
			small	Large	total
Local	Circle with a diameter $\mathcal{D} = 300$ nm	Perfectly Matched Layers (PML) and Perfect Electric Conductor at the edge	0.1 nm	10 nm	42443
Non-Local	Circle with a diameter $\mathcal{D} = 200$ nm	Perfectly Matched Layers (PML) and Perfect Electric Conductor at the edge	0.05 nm	10 nm	139250

Appendix C

Finite element (COMSOL) implementation of the hydrodynamic Drude Model

In 2013, *Yu Luo et al.* [106] introduced a non-local model based on the hydrodynamic Drude model in the frame of conformal transformation. In this model, they intended to find a conformal transformation that would morph a non-local plasmonic system in the real world into a local virtual world. For that, they formulated that the metal is characterized by a spatially dispersive permittivity tensor given by

$$\varepsilon_T(\omega) = \varepsilon_\infty - \frac{\omega_p^2}{\omega(\omega + i\gamma)} \tag{C.1}$$

for transverse electromagnetic fields and

$$\varepsilon_L(\omega, k) = \varepsilon_\infty - \frac{\omega_p^2}{\omega(\omega + i\gamma) - \beta^2|k|^2} \tag{C.2}$$

for the longitudinal electromagnetic fields. Where γ is the metal damping, ω_p is the plasma frequency, β is a non-locality factor proportional to the Fermi's velocity.

In order to avoid the implementation of a k-dependant permittivity, they devised a model that mapped the non-localities into a thin dielectric layer placed on top of the metal boundary. This dielectric layer had to obey the condition

$$\frac{\varepsilon_d}{\Delta d} = \frac{\varepsilon_b \varepsilon_T q_L}{\varepsilon_T - \varepsilon_b}, \tag{C.3}$$

where ε_b is the dielectric constant of the background, ε_d is the permittivity of the dielectric layer, Δd is the thickness of the layer and $q_L = \sqrt{\frac{\omega_p^2}{\varepsilon_\infty} - \omega(\omega + i\gamma)}/\beta$. The other condition is that Δd had to be much smaller than the metal skin depth. In the article they then proved that this is a valid way to solve the non-locality of the optical response of plasmonic structures.

With this, I then altered the Comsol program publicly available by *Toscano et al.* in *http://www.nanopl.org/?page_id=4* and described in [101], to solve this model so that I could use it to compare to the one described in this thesis.

Fig. C.1 and Fig. C.2 show all components of the electric field and current density calculated with the model briefly described here with the implementation from *Toscano et al.* [101] for a circular sector angle $\phi = 0.8rad$. After doing a parameter sweep I am then able to calculate the absorption cross section of the system that is presented in Fig. 4.17.

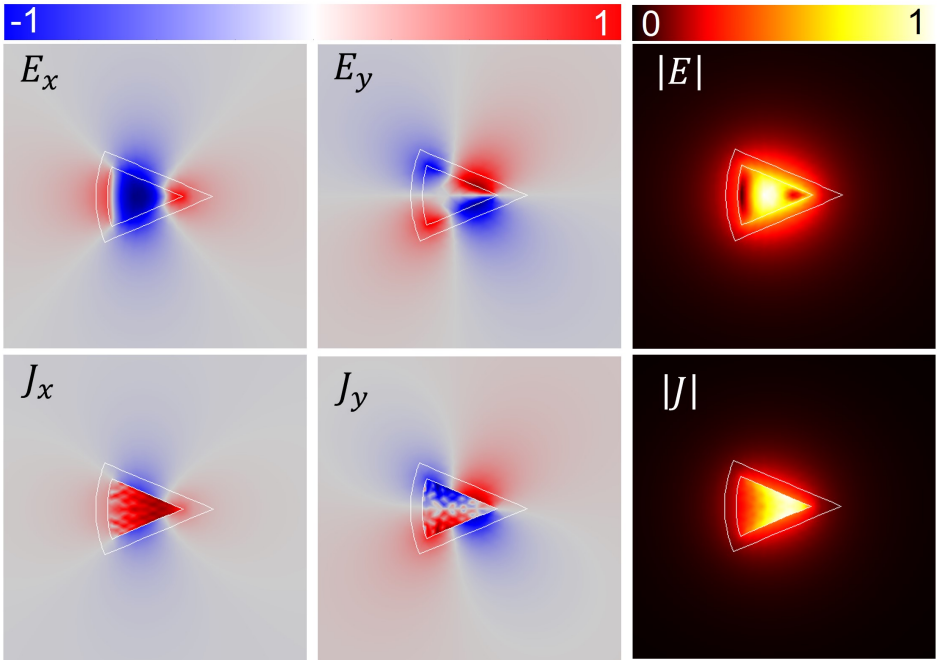

Figure C.1 Solutions to the E_x, E_y, J_x and J_y normalized (left) and to $|E|$ and $|J|$ normalized (right) for the first plasmonic mode using the model described here with the implementation from *Toscano et al.* [101].

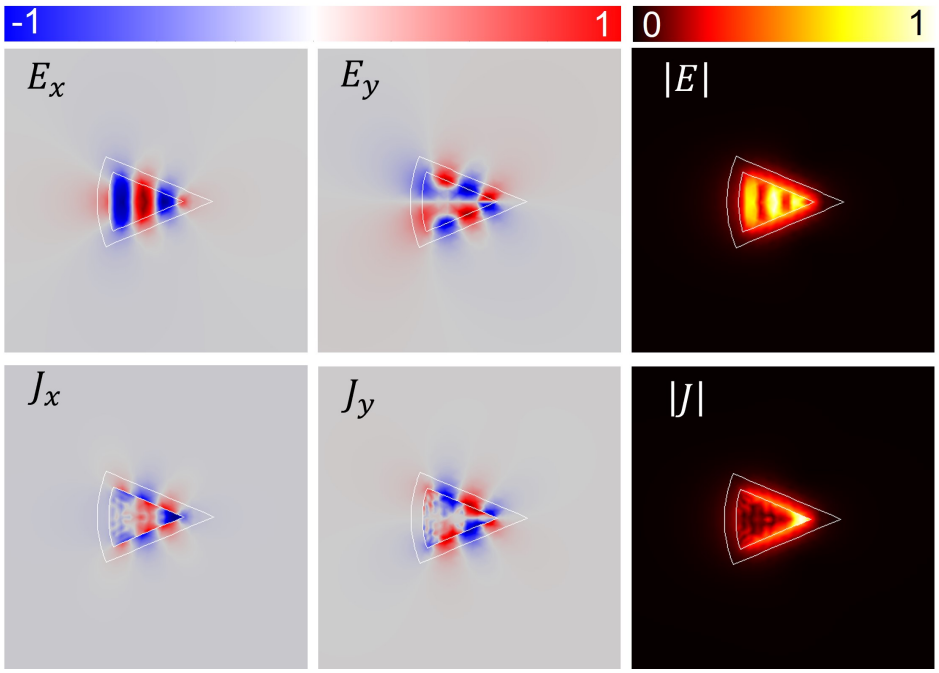

Figure C.2 Solutions to the E_x, E_y, J_x and J_y normalized (left) and to $|E|$ and $|J|$ normalized (right) for the second plasmonic mode using the model described here with the implementation from *Toscano et al.* [101].

List of Figures

List of References

[1] M. Fleischmann, P. Hendra and A. McQuillan, *Raman spectra of pyridine adsorbed at a silver electrode*, Chemical Physics Letters **26** (1974).

[2] A. G. Brolo, *Plasmonics for future biosensors*, Nature Photonics **6** (2012).

[3] H. Moayyed, I. T. Leite, L. Coelho, J. L. Santos and D. Viegas, *Analysis of Phase Interrogated SPR Fiber Optic Sensors With Bimetallic Layers*, IEEE Sensors Journal **14** (2014).

[4] R. Chikkaraddy, B. De Nijs, F. Benz, S. J. Barrow, O. A. Scherman, E. Rosta, A. Demetriadou, P. Fox, O. Hess and J. J. Baumberg, *Single-molecule strong coupling at room temperature in plasmonic nanocavities*, Nature **535** (7610), 127–130 (2016).

[5] A. Demetriadou, J. M. Hamm, Y. Luo, J. B. Pendry, J. J. Baumberg and O. Hess, *Spatiotemporal Dynamics and Control of Strong Coupling in Plasmonic Nanocavities*, ACS Photonics **4** (10), 2410–2418 (2017).

[6] P. Roelli, C. Galland, N. Piro and T. J. Kippenberg, *Molecular cavity optomechanics as a theory of plasmon-enhanced Raman scattering*, Nature Nanotechnology **11** (2), 164–169 (2016).

[7] W. Zhu and K. B. Crozier, *Quantum mechanical limit to plasmonic enhancement as observed by surface-enhanced Raman scattering*, Nature Communications **5** (1), 5228 (2014).

[8] G. Martino, Y. Sonnefraud, S. Kéna-Cohen, M. Tame, Şahin K. Özdemir, M. S. Kim and S. A. Maier, *Quantum Statistics of Surface Plasmon Polaritons in Metallic Stripe Waveguides*, NANOLetters **12** 2504 – 2508 (2013).

[9] M. S. Tame, K. R. McEnery, . K. Özdemir, J. Lee, S. A. Maier and M. S. Kim, *Quantum plasmonics*, Nature Physics **9** 329–340 (2012).

[10] P. G. Kwiat, K. Mattle, H. Weinfurter, A. Zeilinger, A. V. Sergienko and Y. Shih, *New High-Intensity Source of Polarization-Entangled Photon Pairs*, Physical Review Letters **75** 4337–4341 (1995).

[11] H. A. Atwater and A. Polman, *Plasmonics for improved photovoltaic devices*, Nature Materials **9** (3), 205–213 (2010).

[12] M. Liu, T.-W. Lee, S. K. Gray, P. Guyot-Sionnest and M. Pelton, *Excitation of Dark Plasmons in Metal Nanoparticles by a Localized Emitter*, Phys. Rev. Lett. **102** 107401 (2009).

[13] V. Giannini, A. I. Fernández-Domínguez, S. C. Heck and S. A. Maier, *Plasmonic nanoantennas: Fundamentals and their use in controlling the radiative properties of nanoemitters*, Chemical Reviews **111** (6), 3888–3912 (2011).

[14] S. F. Tan, L. Wu, J. K. Yang, P. Bai, M. Bosman and C. A. Nijhuis, *Quantum Plasmon Resonances Controlled by Molecular Tunnel Junctions*, Science **343** (6178), 1496–1499 (2014).

[15] V. Pacheco-Peña, R. A. Alves and M. Navarro-Cía, *Hidden Symmetries in Bowtie Nanocavities and Diabolo Nanoantennas*, ACS Photonics **6** (8), 2014–2024 (2019).

[16] M. Rezaei, P. Rasekh and R. Safian, *A Stripe-Assisted Hybrid Plasmonic Waveguide for the Propagation of Terahertz Waves*, IEEE Photonics Technology Letters **27** (21), 2288–2291 (2015).

[17] S. A. Maier, *Plasmonics: Fundamentals and Applications*. Springer US (2007).

[18] A. V. Kabashin, P. Evans, S. Pastkovsky, W. Hendren, G. A. Wurtz, R. Atkinson, R. Pollard, V. A. Podolskiy and A. V. Zayats, *Plasmonic nanorod metamaterials for biosensing*, Nature Materials **8** (11), 867–871 (2009).

[19] M. Navarro-Cía and S. A. Maier, *Broad-band near-infrared plasmonic nanoantennas for higher harmonic generation*, ACS Nano **6** (4), 3537–3544 (2012).

[20] T. Shoji and Y. Tsuboi, *Plasmonic optical tweezers toward molecular manipulation: Tailoring plasmonic nanostructure, light source, and resonant trapping*, Journal of Physical Chemistry Letters **5** (17), 2957–2967 (2014).

[21] H. Aouani, M. Rahmani, M. Navarro-Cía and S. A. Maier, *Third-harmonic-upconversion enhancement from a single semiconductor nanoparticle coupled to a plasmonic antenna*, Nature Nanotechnology **9** (4), 290–294 (2014).

[22] R. Chikkaraddy, B. De Nijs, F. Benz, S. J. Barrow, O. A. Scherman, E. Rosta, A. Demetriadou, P. Fox, O. Hess and J. J. Baumberg,

Single-molecule strong coupling at room temperature in plasmonic nanocavities, Nature **535** (7610), 127–130 (2016).

[23] F. Benz et al., *Single-molecule optomechanics in "picocavities"*, Science **354** (6313), 726–729 (2016).

[24] D. F. Santos, A. Guerreiro and J. M. Baptista, *Simultaneous Plasmonic Measurement of Refractive Index and Temperature Based on a D-Type Fiber Sensor With Gold Wires*, IEEE Sensors Journal **17** (8), 2439–2446 (2017).

[25] P. Vasa and C. Lienau, *Strong Light-Matter Interaction in Quantum Emitter/Metal Hybrid Nanostructures*, ACS Photonics **5** (1), 2–23 (2018).

[26] E.-P. Li and H.-S. Chu, *Plasmonic Nanoelectronics and Sensing.* Cambridge University Press, 1st Ed. (2014).

[27] C. M. Cobley, S. E. Skrabalak, D. J. Campbell and Y. Xia, *Shape-Controlled Synthesis of Silver Nanoparticles for Plasmonic and Sensing Applications*, Plasmonics **4** (2), 171–179 (2009).

[28] Y. Shen et al., *Plasmonic gold mushroom arrays with refractive index sensing figures of merit approaching the theoretical limit*, Nature Communications **4** (1), 2381 (2013).

[29] M. I. Stockman, *Nanoplasmonics: The physics behind the applications*, Physics Today **64** (2), 39–44 (2011).

[30] P. G. Kwiat, K. Mattle, H. Weinfurter, A. Zeilinger, A. V. Sergienko and Y. Shih, *New High-Intensity Source of Polarization-Entangled Photon Pairs*, Phys. Rev. Lett. **75** 4337–4341 (1995).

[31] R. Esteban, A. G. Borisov, P. Nordlander and J. Aizpurua, *Bridging quantum and classical plasmonics with a quantum-corrected model*, Nature Communications **3** 825 (2012).

[32] D. C. Marinica, A. K. Kazansky, P. Nordlander, J. Aizpurua and A. G. Borisov, *Quantum Plasmonics: Nonlinear Effects in the Field Enhancement of a Plasmonic Nanoparticle Dimer*, Nature Communications **3** 825 (2012).

[33] L. E.-P. and C. H.-S. (eds.), *Plasmonic Nanoelectronics and Sensing*. EuMA High Frequency Technologies Series. Cambridge University Press (2014).

[34] N. Kongsuwan, A. Demetriadou, M. Horton, R. Chikkaraddy, J. J. Baumberg and O. Hess, *Plasmonic Nanocavity Modes: From Near-Field to Far-Field Radiation*, ACS Photonics **7** (2), 463–471 (2020).

[35] S. Lal, S. E. Clare and N. J. Halas, *Nanoshell-Enabled Photothermal Cancer Therapy: Impending Clinical Impact*, Accounts of Chemical Research **41** (12), 1842–1851 (2008). PMID: 19053240.

[36] J. N. Farahani, D. W. Pohl, H.-J. Eisler and B. Hecht, *Single Quantum Dot Coupled to a Scanning Optical Antenna: A Tunable Superemitter*, Phys. Rev. Lett. **95** 017402 (2005).

[37] T. S. van Zanten, M. J. Lopez-Bosque and M. F. Garcia-Parajo, *Imaging Individual Proteins and Nanodomains on Intact Cell Membranes with a Probe-Based Optical Antenna*, Small **6** (2), 270–275 (2010).

[38] L. Novotny and N. Van Hulst, *Antennas for light*, Nature Photonics **5** (2), 83–90 (2011).

[39] H. F. Ghaemi, T. Thio, D. E. Grupp, T. W. Ebbesen and H. J. Lezec, *Surface plasmons enhance optical transmission through subwavelength holes*, Phys. Rev. B **58** 6779–6782 (1998).

[40] C. M. Soukoulis and M. Wegener, *Past achievements and future challenges in the development of three-dimensional photonic metamaterials*, Nature Photonics **5** (9), 523–530 (2011).

[41] T. J. Constant, S. M. Hornett, D. E. Chang and E. Hendry, *All-optical generation of surface plasmons in graphene*, Nature Physics **12** (2), 124–127 (2016).

[42] E. Galiffi, J. B. Pendry and P. A. Huidobro, *Broadband Tunable THz Absorption with Singular Graphene Metasurfaces*, ACS Nano **12** (2), 1006–1013 (2018).

[43] H. Horvath, *Gustav Mie and the scattering and absorption of light by particles: Historic developments and basics*, Journal of Quantitative Spectroscopy and Radiative Transfer (2009).

[44] D. N. Mermin and N. W. Ashcroft, *Solid State Physics*. CRC Press, college Ed. (1976).

[45] B. Gallinet, J. Butet and O. J. Martin, *Numerical methods for nanophotonics: Standard problems and future challenges*, Laser and Photonics Reviews **9** (6), 577–603 (2015).

[46] R. Yu, L. M. Liz-Marzán and F. J. García De Abajo, *Universal analytical modeling of plasmonic nanoparticles*, Chemical Society Reviews **46** (22), 6710–6724 (2017).

[47] F. J. G. De Abajo, *Nonlocal effects in the plasmons of strongly interacting nanoparticles, dimers, and waveguides*, Journal of Physical Chemistry C **112** (46), 17983–17987 (2008).

[48] W. Zhu, R. Esteban, A. G. Borisov, J. J. Baumberg, P. Nordlander, H. J. Lezec, J. Aizpurua and K. B. Crozier, *Quantum mechanical effects in plasmonic structures with subnanometre gaps*, Nature Communications **7** (1), 11495 (2016).

[49] J. D. Cox and F. Javier García de Abajo, *Electrically tunable nonlinear plasmonics in graphene nanoislands*, Nature Communications **5** (1), 5725 (2014).

[50] P. A. D. Gonçalves, T. Christensen, N. Rivera, A.-P. Jauho, N. A. Mortensen and M. Soljačić, *Plasmon–emitter interactions at the nanoscale*, Nature Communications **11** (1), 366 (2020).

[51] C. Ciraci, R. T. Hill, J. J. Mock, Y. Urzhumov, A. I. Fernandez-Dominguez, S. A. Maier, J. B. Pendry, A. Chilkoti and D. R. Smith, *Probing the Ultimate Limits of Plasmonic Enhancement*, Science **337** (2012).

[52] J. M. Pitarke, V. M. Silkin, E. V. Chulkov and P. M. Echenique, *Theory of surface plasmons and surface-plasmon polaritons*, Reports on Progress in Physics **70** (1), 1–87 (2007).

[53] L. Xu and H. Chen, *Conformal transformation optics*, Nature Photonics **9** (1), 15–23 (2015).

[54] F. J. Rodríguez-fortuño, A. Martínez, G. a. Wurtz and A. V. Zayats, *Near-Field Interference for the Unidirectional Excitation of Electromagnetic Guided Modes*, Science **328** (April), 328–331 (2013).

[55] P. A. Huidobro, M. L. Nesterov, L. Martín-Moreno and F. J. García-Vidal, *Transformation optics for plasmonics*, Nano Letters **10** (2010).

[56] J. B. Pendry, A. Aubry, D. R. Smith and S. A. Maier, *Transformation Optics and Subwavelength Control of Light*, Science **337** (6094), 549–552 (2012).

[57] C. Ciracì, R. T. Hill, J. J. Mock, Y. Urzhumov, A. I. Fernández-Domínguez, S. A. Maier, J. B. Pendry, A. Chilkoti and D. R. Smith, *Probing the ultimate limits of plasmonic enhancement*, Science **337** (6098), 1072–1074 (2012).

[58] C. Ciracì, J. B. Pendry and D. R. Smith, *Hydrodynamic model for plasmonics: A macroscopic approach to a microscopic problem*, ChemPhysChem **14** (6), 1109–1116 (2013).

[59] E. Madelung and translated by D.H. Delphenich, *Quantum Theory in Hydrodynamical Form*, Naturwissenschaften (The Science of Nature) **14** 1004–1004 (1926).

[60] R. A. Alves, A. Guerreiro and M. Navarro-Cía, *Bridging the hydrodynamic Drude model and local transformation optics theory*, Phys. Rev. B **101** 235412 (2020).

[61] P. A. Huidobro, M. L. Nesterov, L. Martín-Moreno and F. J. García-Vidal, *Transformation Optics for Plasmonics*, Nano Letters **10** (6), 1985–1990 (2010).

[62] R. Marques, F. Martín and M. Sorolla, *Metamaterials with Negative Parameters: Theory, Design and Microwave Applications* (2008).

[63] L. Solymar and E. Shamonina, *Waves in Metamaterials*. Oxford University Press, Inc., USA (2009).

[64] D. Schurig, J. J. Mock, B. J. Justice, S. A. Cummer, J. B. Pendry, A. F. Starr and D. R. Smith, *Metamaterial Electromagnetic Cloak at Microwave Frequencies*, Science **314** (5801), 977–980 (2006).

[65] E. Houghton, P. Carpenter, S. H. Collicott and D. T. Valentine, *Chapter 6 - Thin Airfoil Theory*, in E. Houghton, P. Carpenter, S. H. Collicott and D. T. Valentine *Aerodynamics for Engineering Students (Seventh Edition)*, 391–447. Butterworth-Heinemann, seventh edition Ed. (2017).

[66] K. Gupta, R. Garg and I. Bahl, *Microstrip Lines and Slotlines*. Artech House (1979).

[67] R. E. Collin, *Field Theory of Guided Waves*. IEEE-Press, second Ed. (1991).

[68] J. Polchinski, *Scale and conformal invariance in quantum field theory*, Nuclear Physics B **303** (2), 226–236 (1988).

[69] T. Levy and Y. Oz, *Liouville conformal field theories in higher dimensions*, Journal of High Energy Physics **2018** (6), 119 (2018).

[70] T. Atay, J.-H. Song and A. V. Nurmikko, *Strongly Interacting Plasmon Nanoparticle Pairs: From Dipole-Dipole Interaction to Conductively Coupled Regime*, Nano Letters **4** (9), 1627–1631 (2004).

[71] H. Duan, A. I. Fernández-Domínguez, M. Bosman, S. A. Maier and J. K. W. Yang, *Nanoplasmonics: Classical down to the Nanometer Scale*, Nano Letters **12** (3), 1683–1689 (2012).

[72] R. W. Taylor, F. Benz, D. O. Sigle, R. W. Bowman, P. Bao, J. S. Roth, G. R. Heath, S. D. Evans and J. J. Baumberg, *Watching individual molecules flex within lipid membranes using SERS*, Scientific Reports **4** (1), (2014).

[73] D. Y. Lei, A. Aubry, Y. Luo, S. A. Maier and J. B. Pendry, *Plasmonic interaction between overlapping nanowires*, ACS Nano **5** (1), 597–607 (2011).

[74] A. Kinkhabwala, Z. Yu, S. Fan, Y. Avlasevich, K. Müllen and W. E. Moerner, *Large single-molecule fluorescence enhancements produced by a bowtie nanoantenna*, Nature Photonics **3** (11), 654–657 (2009).

[75] V. Pacheco-Peña, R. Alves and M. Navarro-Cía, *Hidden Symmetries in Bowtie Nanocavities and Diabolo Nanoantennas*, ACS Photonics **6** (8), 2014–2024 (2019).

[76] V. Pacheco-Peña, R. A. Alves and M. Navarro-Cía, *From symmetric to asymmetric bowtie nanoantennas: electrostatic conformal mapping perspective*, Nanophotonics **9** (5), 1177–1187 (2020).

[77] Y. Luo, J. B. Pendry and A. Aubry, *Surface plasmons and singularities*, Nano Letters **10** (10), 4186–4191 (2010).

[78] L. Novotny and B. Hecht, *Principles of Nano-Optics*. Cambridge University Press (2006).

[79] N. C. Lindquist, P. Nagpal, K. M. McPeak, D. J. Norris and S.-H. Oh, *Engineering metallic nanostructures for plasmonics and nanophotonics*, Reports on Progress in Physics **75** (3), 036501 (2012).

[80] H. Aouani, M. Rahmani, M. Navarro-Cía and S. A. Maier, *Third-harmonic-upconversion enhancement from a single*

semiconductor nanoparticle coupled to a plasmonic antenna, Nature Nanotechnology **9** (4), 290–294 (2014).

[81] H. Shao, H. Im, C. M. Castro, X. Breakefield, R. Weissleder and H. Lee, *New Technologies for Analysis of Extracellular Vesicles*, Chemical Reviews **118** (4), 1917–1950 (2018).

[82] C. Haffner et al., *Low-loss plasmon-assisted electro-optic modulator*, Nature **556** (7702), 483–486 (2018).

[83] T. Christensen, W. Yan, A.-P. Jauho, M. Soljačić and N. A. Mortensen, *Quantum Corrections in Nanoplasmonics: Shape, Scale, and Material*, Phys. Rev. Lett. **118** 157402 (2017).

[84] R. Esteban, A. G. Borisov, P. Nordlander and J. Aizpurua, *Bridging quantum and classical plasmonics with a quantum-corrected model*, Nature Communications (2012).

[85] K. R. Hiremath, L. Zschiedrich and F. Schmidt, *Numerical solution of nonlocal hydrodynamic Drude model for arbitrary shaped nano-plasmonic structures using Nédélec finite elements*, Journal of Computational Physics **231** (17), 5890–5896 (2012).

[86] M. Kupresak, X. Zheng, G. A. E. Vandenbosch and V. V. Moshchalkov, *Comparison of Hydrodynamic Models for the Electromagnetic Nonlocal Response of Nanoparticles*, Advanced Theory and Simulations **1** (12), 1800076 (2018).

[87] A. I. Fernández-Domínguez, A. Wiener, F. J. García-Vidal, S. A. Maier and J. B. Pendry, *Transformation-Optics Description of Nonlocal Effects in Plasmonic Nanostructures*, Phys. Rev. Lett. **108** 106802 (2012).

[88] P. Zhang, J. Feist, A. Rubio, P. García-González and F. J. García-Vidal, *Ab initio nanoplasmonics: The impact of atomic structure*, Phys. Rev. B **90** 161407 (2014).

[89] E. Galiffi, P. A. Huidobro, P. A. D. Gonçalves, N. A. Mortensen and J. B. Pendry, *Probing graphene's nonlocality with singular metasurfaces*, Nanophotonics **9** (2), 309–316 (2020).

[90] S. Lundqvist and N. H. March, *Theory of the Inhomogeneous Electron Gas*. Springer US (1983).

[91] G. Giuliani and G. Vignale, *Quantum Theory of the Electron Liquid*. Cambridge University Press (2005).

[92] R. A. Alves, *Nano-Plasmonics: a stepping stone into Non-linear Quantum Plasmonics*, Msc thesis, Faculdade de Ciencias, Universidade do Porto, Porto (2017).

[93] M. O. Scully and M. S. Zubairy, *Quantum Optics*. Cambridge University Press (1997).

[94] W. Louisell, *Quantum statistical properties of radiation*. Wiley Series in Pure and Applied Optics Series. John Wiley & Sons Canada, Limited (1973).

[95] P. Zhang, J. Feist, A. Rubio, P. García-González and F. J. García-Vidal, *Ab initio nanoplasmonics: The impact of atomic structure*, Phys. Rev. B **90** 161407 (2014).

[96] A. I. Fernández-Domínguez, A. Wiener, F. J. García-Vidal, S. A. Maier and J. B. Pendry, *Transformation-Optics Description of Nonlocal Effects in Plasmonic Nanostructures*, Phys. Rev. Lett. **108** 106802 (2012).

[97] V. Pacheco-Peña, M. Beruete, A. I. Fernández-Domínguez, Y. Luo and M. Navarro-Cía, *Description of Bow-Tie Nanoantennas Excited by Localized Emitters Using Conformal Transformation*, ACS Photonics **3** (7), 1223–1232 (2016).

[98] V. Pacheco-Peña, A. I. Fernández-Domínguez, Y. Luo, M. Beruete and M. Navarro-Cía, *Aluminum Nanotripods for Light-Matter Coupling Robust to Nanoemitter Orientation*, Laser & Photonics Reviews **11** (5), 1700051 (2017).

[99] V. Pacheco-Peña and M. Navarro-Cia, *Understanding quantum emitters in plasmonic nanocavities with conformal transformation: Purcell enhancement and forces*, Nanoscale **10** (2018).

[100] M. Kupresak, X. Zheng, G. A. E. Vandenbosch and V. V. Moshchalkov, *Appropriate Nonlocal Hydrodynamic Models for the Characterization of Deep-Nanometer Scale Plasmonic Scatterers*, Advanced Theory and Simulations **3** (1), 1900172 (2020).

[101] G. Toscano, S. Raza, A.-P. Jauho, N. A. Mortensen and M. Wubs, *Modified field enhancement and extinction by plasmonic nanowire dimers due to nonlocal response*, Opt. Express **20** (4), 4176–4188 (2012).

[102] D. Jin, Q. Hu, D. Neuhauser, F. von Cube, Y. Yang, R. Sachan, T. S. Luk, D. C. Bell and N. X. Fang, *Quantum-Spillover-Enhanced Surface-Plasmonic Absorption at the Interface of Silver and High-Index Dielectrics*, Phys. Rev. Lett. **115** 193901 (2015).

[103] M. Zapata Herrera, J. Aizpurua, A. K. Kazansky and A. G. Borisov,

Plasmon Response and Electron Dynamics in Charged Metallic Nanoparticles, Langmuir **32** (11), 2829–2840 (2016).

[104] C. Ciracì, R. Jurga, M. Khalid and F. D. Sala, *Plasmonic quantum effects on single-emitter strong coupling*, Nanophotonics **8** (10), 1821–1833 (2019).

[105] W. Ding, R. Bachelot, S. Kostcheev, P. Royer and R. Espiau de Lamaestre, *Surface plasmon resonances in silver Bowtie nanoantennas with varied bow angles*, Journal of Applied Physics **108** (12), 124314 (2010).

[106] Y. Luo, A. I. Fernandez-Dominguez, A. Wiener, S. A. Maier and J. B. Pendry, *Surface Plasmons and Nonlocality: A Simple Model*, Phys. Rev. Lett. **111** 093901 (2013).